5-2021

# Centrifugally-Spun Ceramic/Carbon Composite Fibers and Their Use as Anode Materials in Li-Ion Batteries

Gabriel Gonzalez
*The University of Texas Rio Grande Valley*

# CENTRIFUGALLY-SPUN CERAMIC/CARBON COMPOSITE FIBERS AND THEIR USE AS ANODE MATERIALS IN LI-ION BATTERIES

A Thesis

by

GABRIEL GONZALEZ

Submitted to the Graduate College of
The University of Texas Rio Grande Valley
In partial fulfillment of the requirements for the degree of

MASTER OF SCIENCE ENGINEERING

May 2021

Major Subject: Mechanical Engineering

# CENTRIFUGALLY-SPUN CERAMIC/CARBON COMPOSITE FIBERS AND THEIR USE AS ANODE MATERIALS IN LI-ION BATTERIES

A Thesis
by
GABRIEL GONZALEZ

COMMITTEE MEMBERS

Dr. Mataz Alcoutlabi
Chair of Committee

Dr. Horacio Vasquez
Committee Member

Dr. Javier Ortega
Committee Member

May 2021

## ABSTRACT

Gonzalez, Gabriel, Centrifugally-Spun Ceramic/Carbon Composite Fibers and their use as Anode Materials in Li-Ion Batteries. Master of Science Engineering (MSE), May, 2021, 66 pp, 1 table, 34 figures, references, 97 titles.

The work in this thesis focuses on the processing of ceramic/carbon composite fibers via centrifugal spinning for use as anode materials in lithium-ion batteries (LIBs). Due to their high theoretical capacity, abundance, and environmental friendliness, metal oxides have been widely studied as alternate anode materials for lithium-ion batteries. In this research work, we report the synthesis of $SnO_2$:$TiO_2$/ flexible and porous carbon composites ($SnO_2$:$TiO_2$/FPCFs) . When applied as a binder free anode, the (3:2) $SnO_2$:$TiO_2$/FPCFs demonstrated a high theoretical capacity of 900 mAh $g^{-1}$ after 100 cycles at a current density of 100 mA $g^{-1}$. Furthermore, the as prepared ceramic/carbon composite fibers also demonstrated good cycling reversibility after testing at different current rates. For comparison, the results of pure ceramic composites as well as pure FPCFs are also provided.

# DEDICATION

The completion of my master's studies would have not been possible without God, my family, friends, and educators. "Claim to me and I will answer you and tell you great and unsearchable things you do not know". With this biblical verse I want to first thank God for his blessings throughout my personal life and career.

To my mother, Veronica Torres, thank you for your unconditional love, for always providing for me and my sisters, and for teaching me to always maintain a positive attitude towards any circumstance. I will forever be grateful to God for blessing me with such a strong mother, I love you. To my father, Juan Gabriel Gonzalez, thank you for inspiring me to always believe in myself, have good work ethic, and remain humble.

To my grandparents: Francisco Torres, Maria Santa Ramirez, Jesus Gonzalez, Julia Hernandez, thank you all so much for the shared memories, unconditional love, advice, and support. I have much love for all of you and I promise to always keep working hard to represent your teachings and hard work wherever I go.

Finally, to my younger sisters Alondra, and Alejandra, to show you girls that anything is possible with hard work, dedication, and faith.

# ACKNOWLEDGMENTS

I want to thank my committee chair, Dr. Mataz Alcoutlabi for pushing me beyond my limits and showing me that I can do great things. I would also like to thank Dr. Horacio Vasquez and Dr. Javier Ortega for their advice during my undergraduate and graduate studies. Also, thank you to Dr. Karen Lozano for giving me an opportunity to be part of the PREM and for inspiring many students to not be limited by their background.

I would also like to thank my research group “The battery team” for helping me grow professionally and personally. Thank you all for the support throughout my research experience and for making the lab more than just a workplace.

TABLE OF CONTENTS

LIST OF TABLES

LIST OF FIGURES

# CHAPTER I

## INTRODUCTION

The high demand for energy has led to excessive use of fossil fuels which resulted in many environmental issues that are accompanied by a large $CO_2$ emission. Lithium-ion batteries (LIBs) are considered as an alternative energy source to fossil fuel for use in electric vehicles (EVs), electronics and portable devices due to their compact size, high energy density, and high specific lithium storage capacity, [1-3]. Although they have proved outperform other sources of power such as wind and solar energy, LIBs have not yet reached their optimal potential. Currently, the most common anode material used in LIBs is graphite, but it can only deliver a specific capacity of 372 mAh $g^{-1}$ [4-6]. Another limiting factor of graphite is the formation of dendrites on its surface during rapid charging. Such phenomenon leads to low Li-ion diffusivity that can deteriorate the electrochemical performance of the battery[7-9].

Current advancements in nanotechnology have enabled the manufacturing of new nano composites with unique microstructures and morphologies. Due to their distinct characteristics and high surface area, nanocomposites have demonstrated improved performance in a wide variety of applications compared to their bulk counterpart[10-12]. For example, porous, hollow, and tubular are features of the different structures that have been achieved through nanocomposite production methods, which include centrifugal spinning, melt blowing, and electrospinning [13-15].Such morphologies increase the surface area per unit volume of the

material and provide numerous active sites that allow more lithium interaction within the anode during the charge/discharge process. As a result, larger specific capacities and higher energy densities that surpass those of graphite can be obtained. [5, 10]. In the search for alternate anode materials, metals such as Sn, Ti, Fe as well as their respective oxides have been widely investigated as alternate anode materials in LIBs due to their distinct chemical and physical characteristics that can result in high capacities ranging from 500-1000 mAh $g^{-1}$ [16-19]. More recently, nano/micro structured metal oxides have been synthesized through various methods for use as alternate anode materials for LIBs and have exhibited better electrochemical performance when compared to their bulk counterpart. In addition, metal oxides are of interest due to their environmental friendliness, abundance, and low cost[20, 21]. Sn and $SnO_2$ have been widely investigated as an alternate anode material due to their high theoretical capacity of 993.4 mAh $g^{-1}$ and ~782 mAh $g^{-1}$ respectively [22-25]. Despite its high capacity, Sn suffers from a high volume expansion during the alloying/dealloying process with lithium which can result in anode cracking and capacity fading [26-28]. Similarly, $SnO_2$ is brittle material and suffers from huge volume expansion after prolonged charge/discharge cycles leading to pulverization of the anode and poor cycling performance. To improve the electrochemical performance of Sn and $SnO_2$ anodes, the design of new nano/micro-structures and combination with other materials such as $TiO_2$ and carbon have been recently investigated [22-24, 27, 29-31]. $TiO_2$ has been of interest in LIB research for its excellent rate performance, low volume change upon cycling and good capacity retention over long periods of time. When combined with Sn and $SnO_2$, $TiO_2$ forms a unique heterojunction which is well known for its good kinetics and synergistic effect which can result in an improved anode performance [25, 32-37].

Although, Sn/$TiO_2$, and $SnO_2$/$TiO_2$ composites have shown promising results when compared to pure Sn and $SnO_2$, but they still suffer from pulverization after prolonged charge/discharge cycles. To further improve the electrochemical performance of Sn and $SnO_2$, various carbon coating methods have been explored to mitigate the large volume change and stresses during cycling [6, 19, 25, 28, 37-42]. Due to their high porosity and distinct structures, carbon fibers (CFs), have been widely used as stress buffer matrices for metal and metal oxide-based anodes. Compared to their bulk counterpart, CFs, provide larger numbers of reaction cites for Li-ion intercalation that can result in a high anode capacity[43-45].

Currently, electrospinning has been amongst the most used methods to process various composite carbon fibers such as porous, hollow, and multichannel structures and have significantly exhibited promising results when used as stress buffer matrices for metal-oxide anodes. Electrospinning is a process that allows facile fiber production and allows the synthesis of various metal oxide/carbon fibers with distinct nanostructures for LIB and many other applications[46-48]. For example, Haoyi Mou used electrospinning to prepare encapsulated $SnO_2$/$TiO_2$ particles into carbon nanofibers. Tianyu Li et al, synthesized porous carbon nanofibers containing Sn/Ti nanoparticles through electrospinning and subsequent heat treatment. When used as an anode material in LIBs, the Sn/Ti/C composite fibers delivered a capacity of 557 mAh $g^{-1}$ at 100 mA $g^{-1}$ which is higher than that of graphite. Additionally, the as-synthesized composite fibers demonstrated a capacity retention of 98.7 % after 100 cycles at a current density of 50 mA $g^{-1}$ which was attributed to the buffering effect of the flexible carbon-fiber matrix[40, 49-52]. Although good results have been reported using electrospinning, the required high applied voltage as well as long production rates, limit the use of this technology for the high production rate of fibers[48, 53].

More recently, centrifugal spinning has been explored as an alternate method to produce carbon fiber composites. As opposed to electrospinning, centrifugal spinning relies solely on centrifugal forces and high rotational speeds to yield large amounts of fibers [43, 53-55]. Currently, centrifugally spun composite fibers have been used as binder-free anodes in LIB and sodium-ion batteries (SIB) and have exhibited good electrochemical performance[56-58]. Agubra et al synthesized Sn/C composite fibers via centrifugal spinning of Sn/ poly(acrylonitrile) (PAN) precursor solutions followed by a subsequent heat treatment. When applied as a binder-free anode in Li-ion half cells, the Sn/C composite fibers delivered a high reversible capacity of 724 mAh $g^{-1}$ after 50 cycles at a current density of 100 mA $g^{-1}$ which was attributed to the flexible and amorphous structure of the CFs[59]. Work reported on Centrifugally spun $SnO_2$/C composite-fiber anode for SIBs showed that the composite anode delivered a capacity of 158 mA h $g^{-1}$ after 100 cycles at 640 mA $g^{-1}$ and exhibited good rate performance. Though improved electrochemical results have been obtained by centrifugal spinning, such technology still faces some challenges. For example, high loadings of active material (e.g. Sn, Si, Sb nanoparticles) in the precursor solution and uniform distribution of active material within the fibers can be difficult to achieve due to the high viscosity and particle agglomeration in the solution. Although solutions with high viscosity are preferred for centrifugal spinning, compared to electrospinning, the addition of active material to the polymer solution can largely increase the solution viscosity and can negatively affect the formation and the production rate of the composite fibers [56, 60, 61]. To address these issues, different coating methods have been explored to load the active material (e.g., nanoparticles or short fibers) onto centrifugally spun precursor fibers with the aim to improve the anode performance [62, 63].

In the present work, ternary $SnO_2$:$TiO_2$/FPCFs composites were prepared by centrifugal spinning of precursor solutions and subsequent heat treatment. The characterization of the composite fibers was studied by SEM, TEM, XRD, XPS, and TGA. Moreover, when used as a binder-free anode in LIBs, the $SnO_2$:$TiO_2$/FPCFs composite anode with (3:2) $SnO_2$:$TiO_2$ ratio demonstrated outstanding electrochemical results. For comparison, the electrochemical results of $SnO_2$/FPCFs and $SnO_2$:$TiO_2$/FPCFs with (1:1) $SnO_2$:$TiO_2$ ratio were also investigated.

CHAPTER II

LITERATURE REVIEW

## 2.1 The Lithium-ion Battery

The main components in a Lithium Ion Batteries (LIB) are the cathode, the anode, a separator, and a pair of current collectors [64].

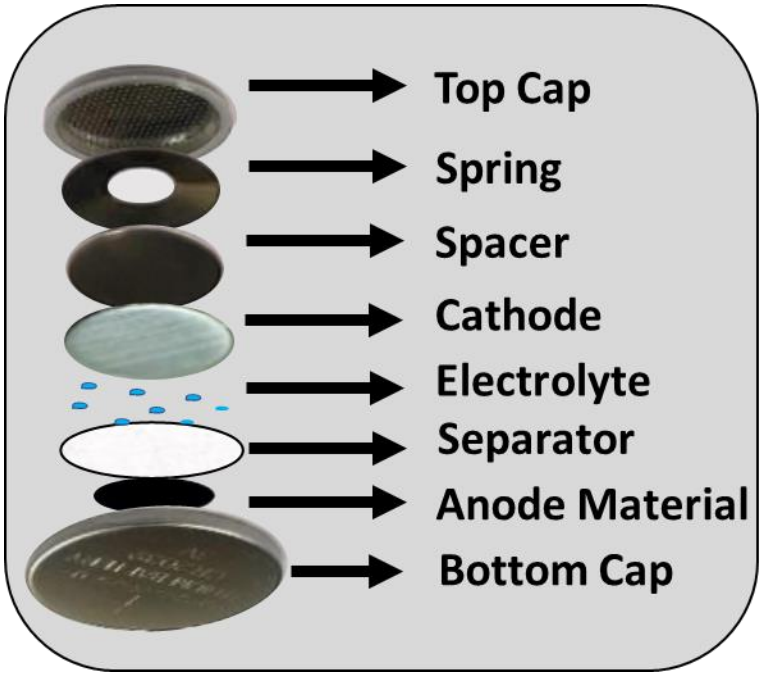


*Figure 1. Schematic of a lithium ion battery coin cell*

The cathode is the positive electrode and the main lithium source of a LIB. The most popular cathodes used in commercial LIBs are materials which have high positive redox potentials such as $LiCoO_2$, $LiMn_2O_4$, and $LiFePO_4$. In the other hand, the anode is the negative electrode and is mainly responsible for dictating the amount of lithium a LIB can retain.

Currently, the most common anode material used in commercial LIB is graphite with theoretical reversible capacity of 372 $mAhg^{-1}$. Both electrodes are divided by an electrolyte filled separator. The separator is usually made from a fiber glass porous enough to allow the transfer of Li-ions between the cathode and the anode yet small enough to prevent the passage of electrons and direct contact between electrodes that can lead to a short circuit. Moreover, the current collectors serve as a conductive path for electrons to transfer from one side to the other and create a current that is supplied to any accessory being powered [16, 65]. The most common current collector material used on the cathode is aluminum due to its stability at high oxidation potentials. On the other hand, the most common current collector material used for the anode is copper due to its excellent stability at low oxidation potentials as well as thermal stability [64].

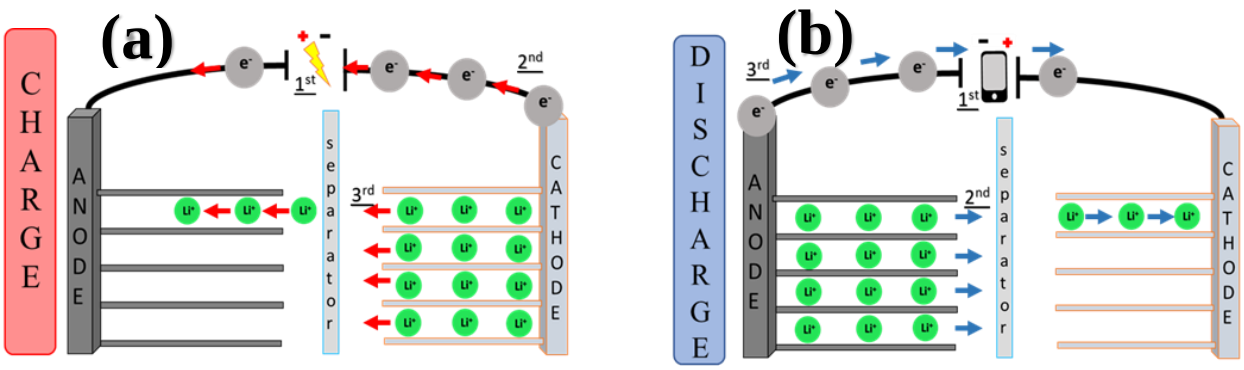


*Figure 2.Working principle of a battery*

### 2.1.1 The Principle of Operation in LIBs

Figure 2 illustrates the process that takes place inside LIBs during the charge (a)/ and discharge (b)discharge cycling process. During the charge process the cathode releases Li Ions that travel through the separator and conductive electrolyte to intercalate into the anode. Vice versa, during the discharge process the Li ions return from the anode to the cathode and complete what is known to be one charge/discharge cycle. Equations 1 and 2 illustrate the two reversible

chemical reactions that occur in the anode and cathode upon charge/discharge cycling, respectively.

Anode:

$$6C + xLi^+ + xe^- \leftrightarrow Li_xC_6 \qquad (1)$$

Cathode:

$$LiCoO_2 \leftrightarrow Li_{1-x}\,CoO_2 + xLi^+ + xe^- \qquad (2)$$

When a full cell is being charged, a significant amount of electrons travel to the anode from the cathode through the current collectors resulting in a reduction and oxidation reaction at the anode and cathode respectively These reactions are reversible and opposite of each other; therefore, during the discharge process the anode oxidizes while the cathode reduces. [4, 16].

## 2.2The Anode Material

The anode material is the negative electrode, and it plays a major role when determining the overall lithium storage of a LIB. While charging/discharging a battery, the anode is responsible for the storage of Li ions and the release of these back into the cathode [4]. An anode electrode must be able to store large amounts of Lithium without pulverizing, form a stable solid-electrolyte interface (SEI) layer, be affordable, and environmentally friendly. Currently, the most common anode material used in commercial LIBs is graphitic carbon. Graphite can best be described as stack of hexagonal sheets of carbon bonded together by van der Waals forces. During the charge process Li ions are inserted in between graphite planes through an intercalation mechanism [16, 66]. Some of the advantages of graphite are its ability to form a controlled and stable SEI layer and its low volume change during insertion/desertion of Lithium while cycling. Although graphite has been an efficient anode material it limits the capacity

storage of LIBs. During lithium intercalation 6 carbon atoms are necessary to intercalate one Li ion. This results in a low theoretical reversible capacity of 372 $mAhg^{-1}$, a small power density, and poor transport rates which are usually less than $10^{-6}cm^{-2}s^{-1}$. To enhance the overall $Li^{+}$ storage an improved anode material that can interact with more Li anodes without pulverizing is required [16, 17, 65].

## 2.3 Alternate Anode Materials

Recent advancements in nanotechnology have paved the road for the synthesis of enhanced nanostructured anode materials. Currently, many nano- and micro- metal oxides and their composites have been widely investigated as alternate anode material in LIBs due to their high lithium capacity, environmental friendliness, and abundance. As opposed to their bulk volume material, nano structured materials have demonstrated different physical and chemical properties that result in an enhanced electrochemical performance. Their small size provides shorter lithium paths and allow a greater surface area to be exposed to the electrolyte. Although outstanding results have been observed in current literature, nanostructured materials still face several drawbacks; therefore, further work is needed in order to ensure safety, stability, and good electrochemical performance

### 2.3.1 Metal Oxides

Synthesizing a material that demonstrates good stability upon cycling has been a major issue for rechargeable LIBs. New alternative electrode materials are needed to improve the efficiency and cyclability of LIBs over prolonged charge/discharge cycles and life shelf [17]. Metal oxides can interact with Li by alloying, insertion, and conversion reaction mechanisms. Metal oxides react with Li through a conversion reaction mechanism and are known to possess

rich and chemical properties that makes them good candidates for anode material. Although metal oxides suffer from low electrical conductivity, thick SEI layer formation, and volume change they can deliver high reversible capacities between 500-1000 $mAhg^{-1}$ [16]. Current advancements in nanotechnology have allowed the synthesis of nano structured metal oxides such as $Fe_2O_3$, $SnO_2$, and $TiO_2$ which have been widely studied as alternate anode material for LIBs due to their unique electrochemical characteristics at the nano level.

### 2.3.2 Iron Oxide based Anodes

Hematite $Fe_2O_3$ is ais a transition metal oxides that has been widely studied as anode material since it isdue to its high theoretical capacity of 1007 $mAhg^{-1}$ . Unlike carbon, one molecule of $Fe_2O_3$ has the capability of interacting with 6 lithium molecules instead of one. The overall reactions of $Fe_2O_3$ with lithium are presented in equations (3,4) [18, 67, 68]. Another characteristic that makes this material attractive is that it can be easily synthesized through different non-hazardous techniques such as hummers salts, sol-gels, and precipitation. Despite its good attributes, $Fe_2O_3$ is susceptible to large internal structural stresses that result in a large volume expansion and lead to poor electrochemical performance over prolonged charge/discharge cycling. Tubular, core shell, and hollow nanostructures are some examples of the different morphologies that have been widely proposed as solutions to mitigate the drawbacks experienced by $Fe_2O_3$. In addition, the creation of different $Fe_2O_3$/carbon composites has also been explored as a method to alleviate the internal stresses experienced by $Fe_2O_3$.

$$Fe_2O_3 + 6Li^+ + 6e^- \rightarrow 2Fe + 3Li_2O \qquad (3)$$

$$Fe_2O_3 + xLi^+ + xe^- \leftrightarrow Li_xFe_2O_3\ (0 \leq x \leq 6) \qquad (4)$$

### 2.3.3 Tin Oxide Anodes

Another metal oxide that has gained much popularity due to its high theoretical capacity of 782 $mAhg^{-1}$ is tin dioxide ($SnO_2$). One major reaction that makes $SnO_2$ interesting is its irreversible reduction process of $SnO_2$ to metallic sn as represented in equation 5 [35]. Such reaction contributes to the irreversible capacity loss during the first charge/discharge cycle; however, it also prevents further pulverization of the material and results in a reversible alloying/dealloying process between Sn and Li as shown in equation 6. This reaction is mainly responsible for the high theoretical capacity of SnO2 which doubles that of graphite.

$$SnO_2 + 4Li^+ + 4e^- \rightarrow Sn + 2Li_2O \qquad (5)$$

$$Sn + xLi^+ + xe^- \leftrightarrow 2Li_xSn\ (0 \leq x \leq 4.4) \qquad (6)$$

However, like most metal oxides, $SnO_2$ faces a large volume expansion and capacity decay upon cycling [35, 69]. This drawback leads to harmful mechanical strains and stresses that are responsible for the pulverization of the anode material and results in a poor electrochemical performance. In order to solve this issue several solutions have been proposed such as hybrid nanostructures, downsizing the particles, and the combination of $SnO_2$ with a material that is less active [41, 70]

### 2.3.4 Titanium Oxide Anodes

Due to their semiconductive, photolytic, and electrochemical characteristics, $TiO_2$ composites are amongst the most popular metal oxides that have been studied in the fields of energy storage, chemical sensing, as well as in biomedical applications[12, 71]. Furthermore, their low cost, abundance, and environmental friendliness are also properties of $TiO_2$ nanocomposites to be considered for numerous battery and gas sensing applications [34, 36, 72,

73]. More recently, $TiO_2$ has been widely used in LIB application due to its great rate capabilities and cyclic stability upon cycling. When combined with other materials such as Sn, $SnO_2$, and Fe, $TiO_2$ is known to mitigate the tremendous volume expansion; however, if used in excess it can hinder the overall capacity of the synthesized composite due to its low theoretical capacity of 323 mAh $g^{-1}$. The interaction of $TiO_2$ and lithium can be chemically represented by the following equation.

$$TiO_2 + xLi^+ + xe^- \leftrightarrow Li_xTiO_2\ (0 \leq x \leq 1) \qquad (7)$$

### 2.4 Centrifugal Spinning

Centrifugal spinning is a new method that has been gaining popularity in the aera of nano/micro fiber processing and formation [44, 57, 74]. Unlike electrospinning, centrifugal spinning does not depend on high voltage and electric field to produce nano and micro composite fibers. Instead, centrifugal spinning depends solely on centrifugal forces caused by the spinneret rotational speed to produce nano and microfibers with high yield and in a short period of time[43, 75, 76]. However, high loadings and uniform distribution of active material within the fibers can be difficult to achieve due to the high viscosities and particle agglomeration when preparing solutions and during the spinning process, respectively. Although viscous solutions are preferred for this process, the addition of nanoparticles can largely increase the viscosity of a solution and impact the fiber production feasibility as well as the production rate. To resolve these issues, different coating methods have been explored to load nanoparticles onto centrifugally spun fibers and increase their electrochemical performance when used as anode material for LIBS.

CHAPTER III

EXPERIMENTAL PRODEDURES

## 3.1 State of the art equipment

The investigation to design an improved flexible binder free metal oxide microfiber anode will require the use of the following state of the art software and hardware equipment.

*Figure 3.Cyclone Machine*

The cyclone machine is a new technology owned by The University of Texas Rio Grande Valley. It is a machine that uses angular velocity and centrifugal forces to produce microfibers. This machine will be used to produce polymer precursor metal oxide microfibers. The varying parameters are the humidity and temperature of the room while the controllable parameters are the speed and time per cycle.

*Figure 4.Vacuum Oven*

The Vacuum Oven in Figure 4 will be used to store and dry under vacuum the obtained microfibers overnight. This is a crucial step in the overall process since it assures the evaporation of any leftover solvents and prevents any moisture from damaging the fibers.

*Figure 5. OTF-1200X Furnace*

The furnace illustrated in Fig 5 will be used to oxidize the obtained precursor metal oxide microfibers and to also carbonize them under an argon environment. The equipment is attached to an argon tank with a flowmeter and regulator that are used to control the amount of argon flowing through the tube. The obtained carbonized fibers are then cut into circular ½ inch diameter anodes and assembled into coin cells to perform an electrochemical study.

*Figure 6. MBraun Lab star pro glove box*

Figure 6 shows the Mbraun Lab star pro glove box under argon environment which will be to assemble the obtained carbonized metal oxide microfiber anodes into lithium ion battery half cells.

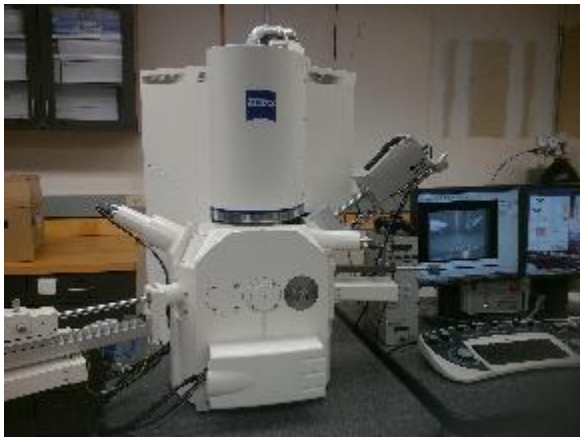

*Figure 7. Scanning Electron Microscope (SEM) and Energy Dispersive X-ray Analysis (EDAX)*

The SEM instrument will be used to characterize the structure and surface morphology of the obtained polymer precursor and carbonized metal oxide microfibers. It is important to note that this SEM instrument is equipped with an Energy Dispersive X-ray Analysis (EDAX) instrument that will be used to determine the elemental composition of the metal oxide composite microfibers.


*Figure 8. TG 209 Tarsus (TGA) Instrument*

The TG 209 Tarsus is a thermogravimetric analysis (TGA) instrument that will be used to confirm the amount of metal oxide material within the obtained microfiber.

*Figure 9. BioLogic Cyclic Voltammetry (CV) Instrumentation*

The CV instrumentation will be used to study the oxidation/reduction reactions that will be happening in the metal oxide composite anode. This machine will be operated with a scan rate of 0.2 mV/s between 0 and 3 V at a frequency of 0.1 Hz and 1kHz respectively. The instrument will be connected to a computer equipped with BTLab which will be used to configure and observe the ongoing experiments.


*Figure 10. Autolab 128 N Electrochemical Impedance Spectroscope*

The Autolab 128 N Electrochemical Impedance Spectroscope will be utilized to study the electrolyte and interfacial resistance for comparison of cycled and uncycled cells. This instrument will be connected to a computer equipped with eh Nova 1.10 software which will serve to set up, run, and display experiments.

*Figure 11. LANHE Battery Testing System*

The LANHE Battery Testing System illustrated in figure 11 will be used to study the charge/discharge performance, columbic efficiency, and cyclic stability of the metal oxide composite microfiber anodes at different current densities over a charge/ discharge voltage of 3V and 0.05 V respectively. This machine will be connected to computer with a monitor equipped with  LAND Battery Testing Monitor system software which will be used to set up and display the ongoing experiment.

*Figure 12. Arbin Battery Testing System*

Figure 12 displays the Arbin Battery Testing System which will be used to further analyze the performance and stability of the metal oxide composite anodes at different current rates set according to the anode's weight. The instrument will be connected to a computer and monitor that will be used to configure the desired settings of the experiment as well as to display and import results.

## 3.2 Fabrication of fiber composites

For the processing of the short fibers, Absolute ethanol (200 proof), Polyvinylpyrrolidone (PVP) with average molecular weight (MW) of 1,300,000 (99.5%), Tin II 2ethylhexanate (92.5-100%), Titanium IV butoxide (97%), Polyacrylonitrile with average Mw of 150,000, N, N-Dimethyl Formamide (DMF), SuperP carbon black and Poly methyl methacrylate (PMMA) were all purchased from Sigma-Aldrich and used without further modification.

### 3.2.1 Ceramic composite fibers anode preparation

Short metal-oxide microfibers were synthesized through the calcination of centrifugally spun precursor fibers. Briefly, 3 g of PVP were dissolved in 17 g of ethanol and the solution was stirred for 12 h at room temperature. Subsequently, 1.5 g of Tin(II) 2 ethylhexanate was added to the solution and the mixture was stirred for an additional 12 h to obtain a homogeneous solution. The solution was centrifugally spun at 9000 RPM with a relative humidity of 55% to prepare the precursor fibers. The pristine precursor fibers were heated in air at 700 °C for 3 h with a heating rate of 2 °C /min to yield $SnO_2$ short fibers. To obtain pure $TiO_2$ precursor fibers, the same process was used. Initially, 1.5 g of Titanium (IV) butoxide was added to prepare the precursor solution. The process was used to obtain the $SnO_2/TiO_2$ composite precursor solutions which were labeled as $SnO_2/TiO_2$ (3:2) and $SnO_2/TiO_2$ (1:1). To prepare anodes from the pure ceramic fibers first, the as prepared $SnO_2/TiO_2$ nanocomposites, with a ratio of 3:2, were crushed in a mortar and pestle, then 80 % of the short fibers, 10 % PAN, and 10 % carbon black were mixed in 1g of DMF to prepare a slurry. To obtain homogeneity, the as-prepared slurry was sonicated for 30 minutes and subsequently stirred for 12 hours. Subsequent to homogenization, the slurry was coated onto a copper foil and dried under vacuum at 60 °C for 24 hours. Once dry the coated slurry was heat treated in an argon filled tube furnace at 450 °C for 5 hours with a heating rate of

2 °C/min. After heating 0.5” circles were cut to be tested as an anode material. The processing method of the short metal oxide micro-fibers is shown in Figure 13 and the anode preparation is illustrated in Figure 14.

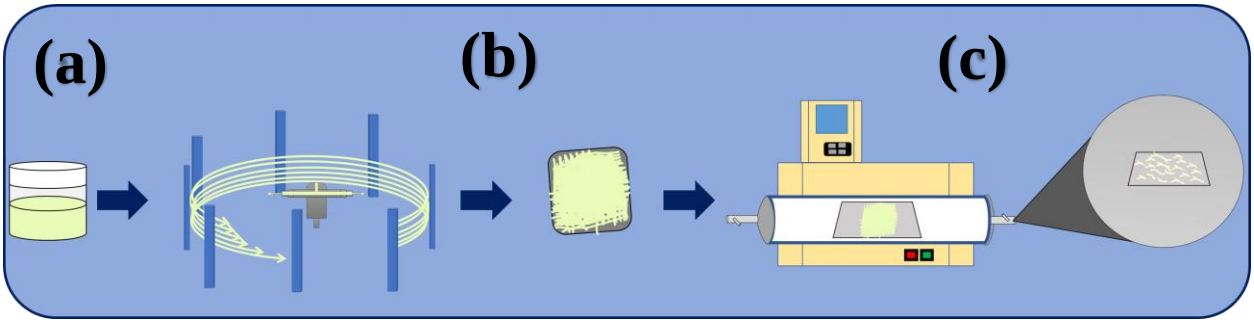


*Figure 13. A schematic representation of metal-oxides fiber fabrication process: (a) polymer solution with metal-oxide precursors, (b) centrifugal spinning, and (c) calcination.*

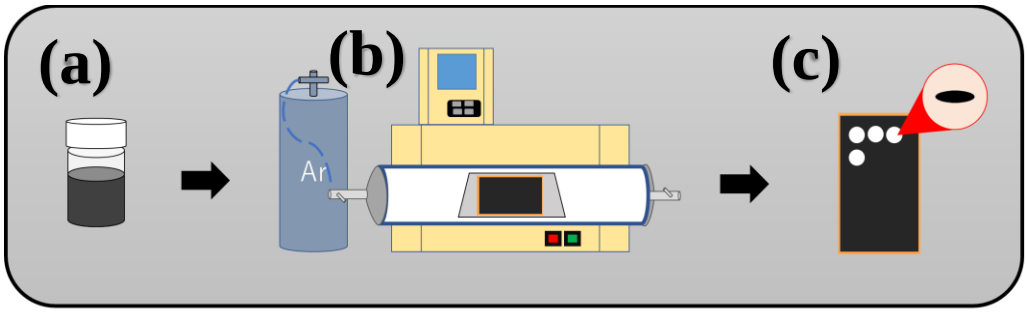


*Figure 14. Schematic representation of short fibers slurry(a) heat treated at 450 C in argon (b) and (c) anode preparation.*

### 3.2.2 Ceramic/carbon composite fibers anode preparation

1.92 g of PAN were dissolved in 17.6 g of DMF by magnetically stirring for 12 h to prepare a homogeneous. Then, 0.48 g of PMMA was added while the solution was left to stir for an additional 12 h at 60 °C. The PAN/PMMA solution was then loaded into a 3 mL syringe and fed into a spinneret to prepare centrifugally spun PAN/PMMA pristine fibers at 8500-9000 RPM with a relative room humidity of 55-60 %. The obtained precursor fibers were then dried under vacuum overnight at 60 °C to evaporate any remaining solvent. Prior to preparing the coating solution, TGA was conducted on the PAN/PMMA fibers to determine the amount of carbon yield after carbonization at 700 °C [77]. The coating solution was then prepared by mixing 50 wt% of short micro-belt fibers, with (3:2) ($SnO_2$/ $TiO_2$) ratio in ethanol followed by sonication (1 h) and magnetic stirring for 24 h. The coating solution was then loaded into a 3ML syringe and was manually coated onto the pristine PAN/PMMA fibers. The coated fibers were then dried under vacuum at 60 °C for 24 h to evaporate any remaining solvent. To obtain flexible ternary $SnO_2$/ $TiO_2$/C composite fibers, the metal oxide coated precursor fibers were stabilized in air at 280 °C for 6 h (heating rate of 3 °C/min) and carbonized at 700 °C for 3 h in an argon filled tube furnace (heating rate of 5 °C/min). To prepare pure FPCFs, the same heat treatment was applied to PAN/PMMA pristine fibers. The obtained carbon fibers were cut into 0.5- discs and used as binder-free anodes in LIBs. This process can be represented by figure 15.

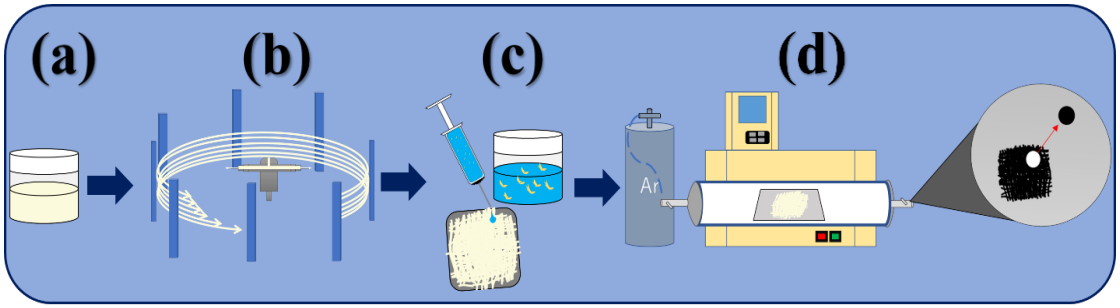


*Figure 15. Schematic representation of ceramic/fiber composite anodes fabrication (a)polymer blend solution, centrifugal spinning process (b), coating technique (c), and subsequent heat treatment (d)*

## 3.3 Electrochemical Evaluation

### 3.3.1 Cell preparation and electrochemical testing

The as-prepared 0.5" $SnO_2$ and $SnO_2/TiO_2$ ceramic/carbon fiber-e anodes were placed in an argon filled glove box ($O_2$, $H_2O$ concentrations < 0.5 ppm MBRAUN, (USA). Li-ion half cells (CR 2032 (PHD Energy Inc.)), with Li-metal as the counter electrode and glass microfibers as the separator, . The electrolyte was prepared from1M li$PF_6$ in ethylene carbonate (EC)/ dimethyl carbonate (DMC) (1:1 v/v) and used without any further additives. Cyclic voltammetry experiments were performed at a scan rate of 0.2 mV $s^{-1}$ over a voltage range between 0.05 and 3.0 V using Biologic Science Instruments (France).. The electrochemical performance of the anodes was evaluated by galvanostatic charge-discharge experiments using a LANHE battery testing system (CT2001A) with an applied current density of 100 mA $g^{-1}$ over 70 cycles for the ceramic composites and 100 cycles for the carbonized composites in a potential range of 0.05 – 3.0 V. The rate capability of the composite-fiber anodes was studied using ARBIN with a current density 50 mA $g^{-1}$, 100 , 200, 400, 500, and 50 mA $g^{-1}$ for 10 cycles each.

# CHAPTER IV

# RESULTS AND DISCUSSION

## 4.1 Characterization of ceramic/carbon composites

The precursor fibers were prepared by centrifugal spinning using a FiberLab L1000 (FibeRio) operated at different spinneret rotational speeds. The morphology and elemental composition of the fibers were studied using scanning electron microscope (SEM) using a Sigma VP Carl Zeiss instrument, equipped with an energy dispersive x-ray spectrometer (EDS) from EDAX (Mahwah, NJ, USA)). The thermal behavior of the precursor fibers was investigated by thermogravimetric analysis (TGA) in air environment with temperatures from 50 to 700 °C with a heating rate of 5 °C /min. X-ray diffraction (XRD) and x ray photoelectron spectroscopy (XPS) analyses were performed to determine crystal structure/crystallization phase of the oxidized fibers and the surface chemistry of the fibers. The XRD patterns were studied using a Rigaku Miniflex II X-ray Diffractometer equipped with a copper source ($K_\alpha$ x =1.54Å). The XPS spectrum were collected using Thermoscientific K-α instrument equipped with monochromatized Al Kα radiation (1486.7 eV). Transmission electron microscopy (TEM) images and selected area electron diffraction (SAED) images were captured using a FEI G2 F30 microscope with a working voltage of 300 kV. The High-angle annular dark field (HAADF) scanning TEM (STEM) and EDS maps were acquired with a FEI G2 Titan 60-300 probe corrected microscope equipped with a Super-X EDS system. The Titan was used at 200 kV with a convergence and a HAADF inner collection semi angles of 24mrad and 58.6 mrad, respectively.

### 4.1.1 Ceramic composite fibers

Figure 16 shows the SEM images of the $TiO_2$ (a-c), $SnO_2$ (d-f), $SnO_2/TiO_2$ (1:1) (g-i), $SnO_2/TiO_2$ (3:2) (j-l) synthesized nano/micro systems obtained after calcination at 700 °C. As it can be seen in Figure 16, the SEM images show short-microfibers morphology. The $TiO_2$ sample (Fig. 16 (a)) exhibits short fiber porous structure and rough surface composed of spherical particles. On the other hand, the SEM images of the $SnO_2$ fibers (Figure 16 (d-f)) depict a short fiber morphology with smoother surface and spherical particles randomly embedded in the surface. The $SnO_2/TiO_2$ (1:1) composite fibers, also adhere a short-fiber structure morphology with interconnected particles on their surface as can be seen in Figure 16 (g-i). In comparison, the $SnO_2/TiO_2$ (3:2) composite fibers show a new microstructure which can be observed in Figure 16(j-l). The SEM images of the $SiO_2/TiO_2$ (3:2) composite reveals a short micro belt-fiber structure with spherical particle randomly distributed on the surface.

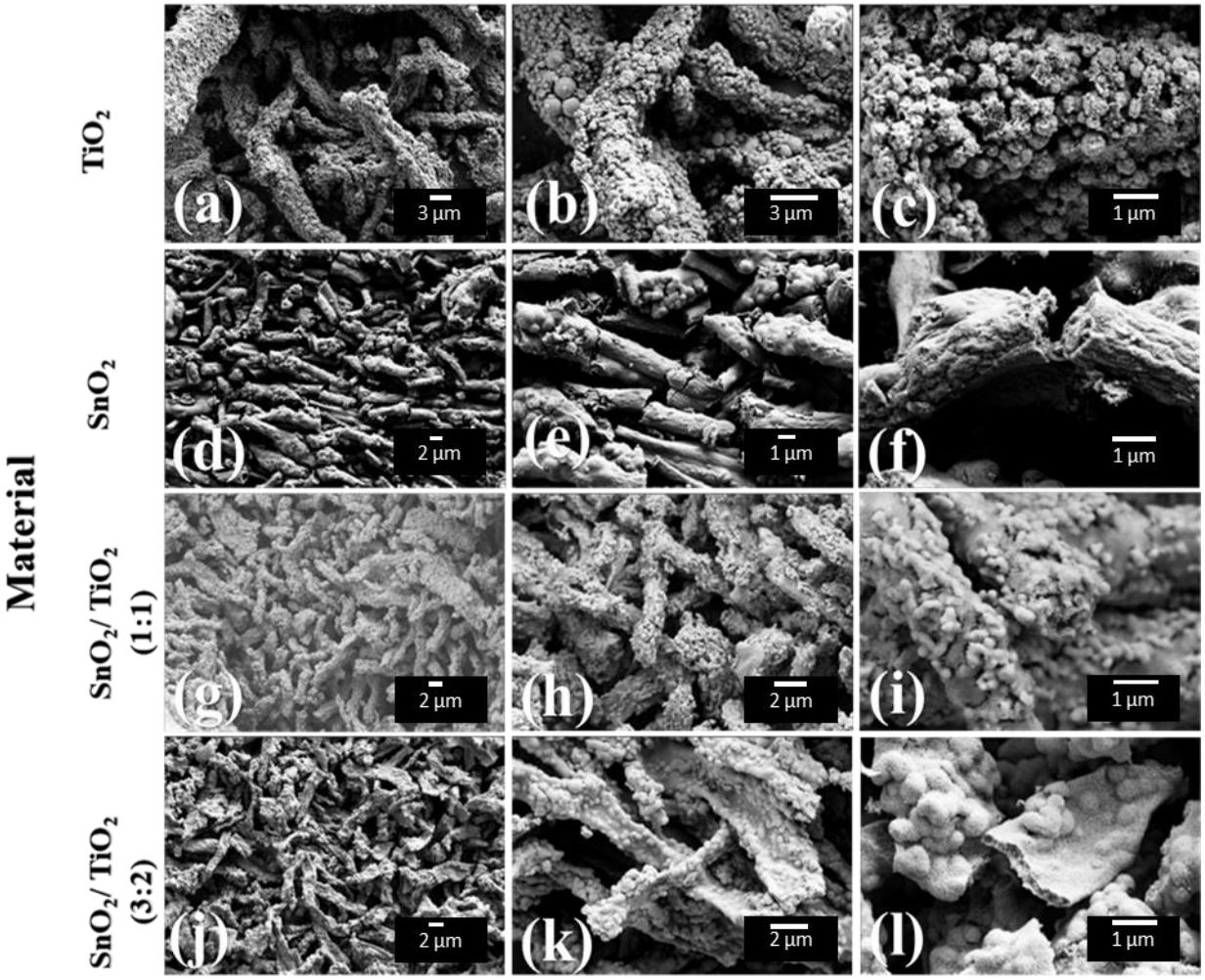


*Figure 16.SEM images of $TiO_2$ (a, b, c), SnO2 (d, e, f), (1:1) (g, h, i), and $SnO_2/TiO_2$ (3:2) (j, k, l), after calcination at 700°C. Magnification: (a, d, g, j) 2000 x, (b, e, h, k) 5,000 x and (c, f, i, l) 10,000 x.*

The elemental composition of the composite microfibers was studied by EDS and is shown in Figure 17 (a-d). Sn, Ti, and O can be observed to be highly present within the elemental composition of each corresponding sample. It can be seen in Figure 17 (a) that the $TiO_2$ sample exhibits a high content of 80 wt. % of Ti while the $SnO_2/TiO_2$ composites with 1:1 and 3:2 ($SnO_2$:$TiO_2$) ratios only depict 25 and 18 wt. % of Ti, respectively. Additionally, the pure $SnO_2$ sample (Figure 17 (b)) shows 90 wt. % of Sn while the $SnO_2/TiO_2$ composites with 1:1 and 3:2 ($SnO_2$:$TiO_2$) ratios only demonstrate 52 and 54 wt. % of Sn, respectively. The small

amount of Ti and Sn within the $SnO_2/TiO_2$ composite-fiber samples with 1:1 and 3:2 ($SnO_2$:$TiO_2$) ratios are ascribed to the successful mixing of $SnO_2$ and $TiO_2$ precursors used to prepare the composite fibers with distinct morphologies. Furthermore, the EDS spectrum of all samples also exhibits signal peaks of oxygen, which confirm the presence of $SnO_2$ and $TiO_2$ in the as-synthesized samples. Moreover, carbon and nitrogen signals can also be observed in all samples. However, such insignificant signals found in the elemental composition can be attributed to precursor impurities, carbon residue from the PVP, and the carbon tape used during sample preparation [78].

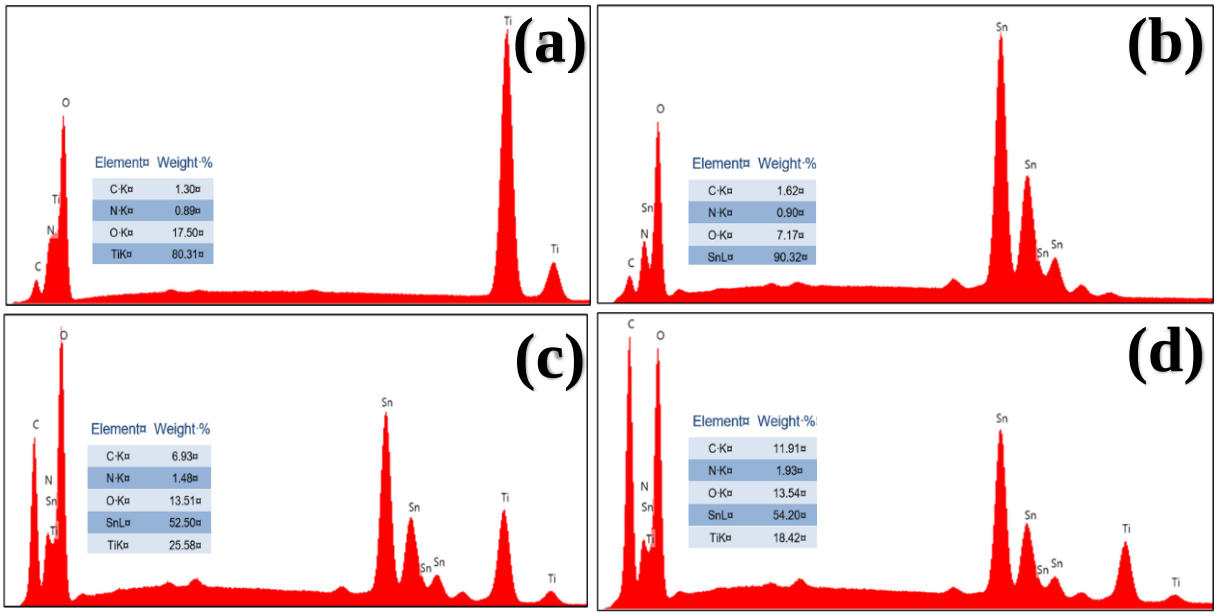


*Figure 17. EDS spectrum of $TiO_2$ (a) $SnO_2$ (b), $SnO_2/TiO_2$ (1:1) (c), and $SnO_2/TiO_2$ (3:2) (d) after calcination at 700 °C.*

Figure 18 (a) shows the TGA results of the composite precursor fibers as well as the XRD (b) of the fibers. As can be seen in the figure, all composite precursor fibers have two main weight loss -steps observed in two different temperature ranges. The first weight loss was observed in the rage of 25 -100 °C which can be attributed to the loss of either remaining solvent or water adsorbed within the fibers. The second observed weight loss between 300 and 550 °C

can be associated with the degradation of the polymer and ceramic precursor-fibers. At the temperature range between 560 and 700 °C, the samples show stable and constant average of residual weight of 10 wt. %, which was attributed to the formation of $SnO_2$, $TiO_2$, and $SnO_2/TiO_2$ composites as well as carbon residue, impurities from the polymer. Figure 4b shows diffraction patterns for the $SnO_2$ (i), $TiO_2$ (ii), $SnO_2/TiO_2$ (1:1) (iii), and $SnO_2/TiO_2$ (3:2) (iv) short microfibers. The$SnO_2$ (i) and $TiO_2$ (ii) samples have similar lattices which was the P42/M space group and each lattice has different lengths to the sides of the unit cell. The results of the Le Bail fitting is shown in Table 1 which indicate that a good fitting was obtained between the known structure of $TiO_2$ and $SnO_2$ and the synthesized samples; the GOF is indicated by a $\chi^2$ value of less than 5. The $TiO_2$ diffraction pattern showed peaks at 2 q of 32.1, 42.3, 45.8, 48.3, 51.6, 64.3, 67.0, 74.6, and 76.1°. These diffraction peaks correspond to the 110, 101, 200, 111, 210, 211, 220, 002, 310, 221 diffraction planes for the rutile phase of $TiO_2$. The diffraction pattern for the $SnO_2$ (Figure 18b (i)) showed diffraction peaks at 31.0, 39.7, 44.6, 45.6, 61.00, 64.8, 68.9, 73.6, 74.3, 77.1 and 78.8°, which correspond to the 110, 101, 200, 111, 210, 21, 220, 002, 310, 221, 112, 301 diffraction planes. The XRD patterns of the $SnO_2/TiO_2$ short fibers showed diffraction peaks at 31.2, 40.3, 44.5, 61.7, 65.0, 74.00 and 78.5° which correspond toto a combination of the diffraction planes observed for the $SnO_2$ and $TiO_2$ materials. The fitting results confirmed both rutile ($TiO_2$) and $SnO_2$ [79-81] [82, 83]. In addition, the observed diffraction peaks in the composite-fiber samples were broad and relatively weak, indicating a smaller particle size for both $TiO_2$ and $SnO_2$ when compared to the individual particles of $TiO_2$ and $SnO_2$.

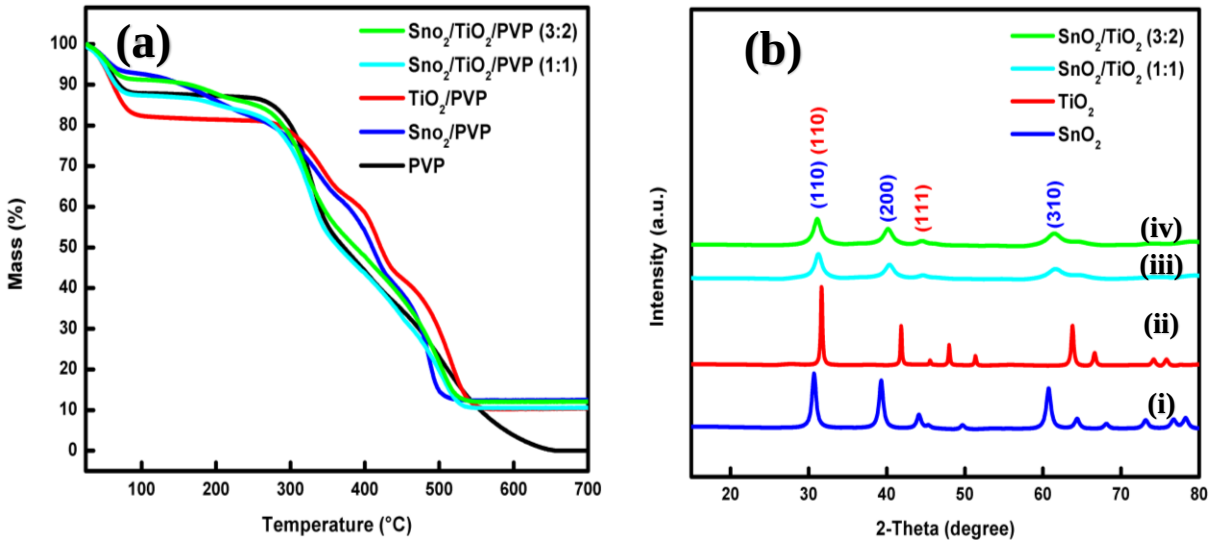


*Figure 18. TGA (a) of PVP and pristine fibers before calcination, XRD (b), of $TiO_2$ (i), $SnO_2$ (ii), $SnO_2/TiO_2$ (1:1) (iii), and $SnO_2/TiO_2$ (3:2) (iv) after calcination at 700 °C.*

**Table 1:** Le Bail fitting $SnO_2$, $TiO_2$ and $SnO_2/TiO_2$ samples

| **Sample** | **Phase** | **Space Group** | **a(Å)** | **b(Å)** | **c(Å)** | **α(°)** | **β(°)** | **γ(°)** | **$\chi^2$** |
|---|---|---|---|---|---|---|---|---|---|
| $SnO_2$ 700°C | $SnO_2$ | P 42/m n m | 4.732(7) | 4.732(7) | 3.132(9) | 90.00 | 90.00 | 90.00 | 2.44 |
| $TiO_2$ 700°C | $TiO_2$ | P 42/m n m | 4.589(9) | 4.589(9) | 2.957(2) | 90.00 | 90.00 | 90.00 | 3.04 |
| | $TiO_2$ | P 42/m n m | 4.600(2) | 4.600(2) | 2.98(2) | 90.00 | 90.00 | 90.00 | |
| $SnO_2/TiO_2$ 700°C 1:1 | $TiO_2$ | P 42/m n m | 4.518(1) | 4.518(1) | 2.959(2) | 90.00 | 90.00 | 90.00 | 2.08 |
| | $SnO_2$ | P 42/m n m | 4.7454(4) | 4.745(4) | 3.130(9) | 90.00 | 90.00 | 90.00 | |
| $SnO_2TiO_2$ 700°C 3:2 | $TiO_2$ | P 42/m n m | 4.544(2) | 4.544(2) | 2.950(0) | 90.00 | 90.00 | 90.00 | 1.82 |
| | $SnO_2$ | P 42/m n m | 4.741(6) | 4.741(6) | 3.133(9) | 90.00 | 90.00 | 90.00 | |

X-ray photoelectron (XPS) characterization was performed to determine the compositions and chemical states of the elemental components in the as synthesized samples. The and XPS survey spectrum for each sample is shown in Figure 19 (a-d), which shows the presence of Sn and O as the major components in the $SnO_2$ sample and some residual C from the sample preparation. The XPS spectrum of the $TiO_2$ fibers shows the presence of Ti and oxygen as the main portions of the sample with some residual carbon left from the synthesis. The $TiO_2$/ $SnO_2$ composite-fiber samples consisted of Ti, Sn and O as well as a small amount of C residue from the sample preparation.

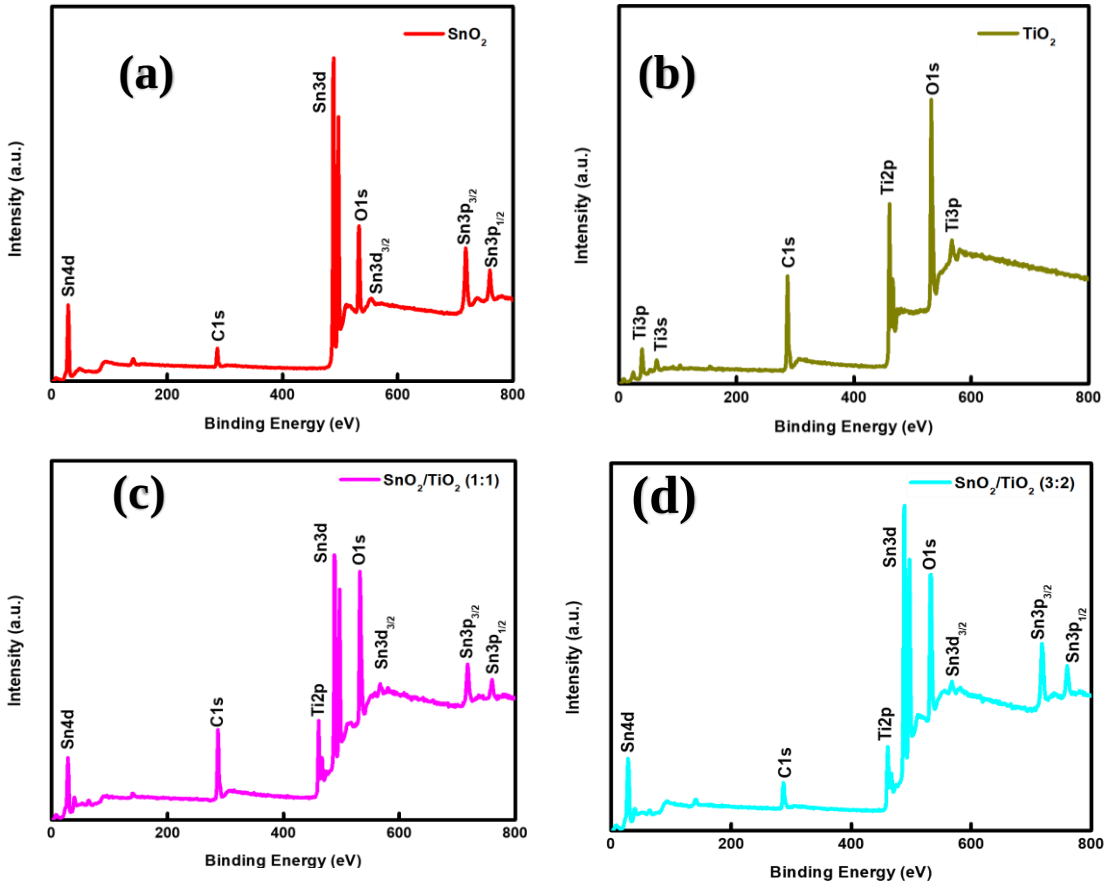


*Figure 19. XPS surveys for the $SnO_2$ oxidized short fibers at 700°C (a), $SnO_2$:$TiO_2$ with a ratio of 1:1 (b), and $SnO_2$:$TiO_2$ at a ratio of 3:2 (c).*

.

Figure 20 shows the Sn $3d_{5/2}$ and $3d_{3/2}$ peaks, which are located around 487 eV and 496 eV, respectively. Figure 20 (a) shows the spectrum for the $SnO_2$ oxidized at 700°C the spectrum can be deconvolved into 2 peaks. In the Sn $3d_{5/2}$, a small peak is observed at 487 eV indicating the presence of Sn (IV) [84-86]. The second peak observed in the spectrum is the $Sn3d_{3/2}$ fitting which was located at 495.2 eV again indicating the presence of Sn (IV) in the sample. Figure 20 (b) and (c) show the XPS spectrum of the oxidized $SnO_2/TiO_2$ composite fibers with a ratio of 1:1 and 3:2, respectively. The XPS results in Figure 6 b and c showed the presence of Sn $3d_{5/2}$.

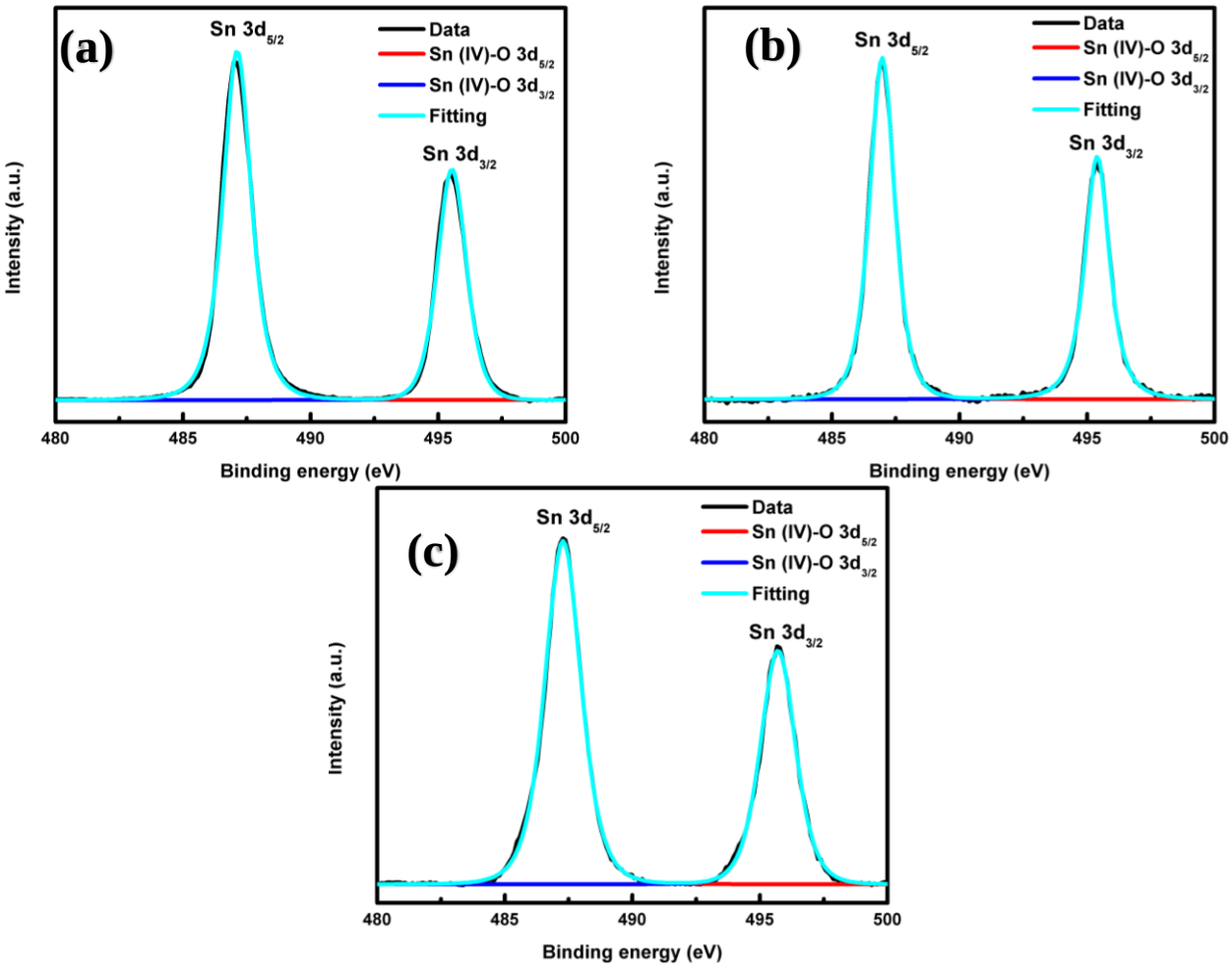


*Figure 20. Sn 3d XPS for the $SnO_2$ oxidized short fibers at 700°C (a), $SnO_2$:$TiO_2$ with a ratio of 1:1 (b), and $SnO_2$:$TiO_2$ at a ratio of 3:2(c).*

.

Figure 21 (a) shows the Ti $2P_{5/2}$ and $Ti2P_{3/2}$ XPs regions for the $TiO_2$ and $SnO_2/TiO_2$ composite-fiber samples after heat treatment at 700°C. Figure 21 (a) shows the $Ti_2P$ XPS spectrum for the pristine $TiO_2$ fibers oxidized at 700 °C which was deconvolved into three peaks located at 459.2, 464.9 eV and 472.6 eV. The peaks located at 459.2 and 464.9 eV are the Ti $2P_{5/2}$ and $Ti2P_{3/2}$ and confirm the presence of Ti as Ti(IV) in the $TiO_2$ fibers [86-88]. The third peak located around 472.6 eV was determined to be the Ti 2P satellite feature [86, 88]. In addition, the $SnO_2/TiO_2$ (1:1) and (3:2) show the same peaks with the same energies indicating the presence of Ti in all the fibers contained Ti(IV) as $TiO_2$. Figure 21 (b) and (c) show the Ti 2P spectrum for the $SnO_2/TiO_2$ composite fibers with $SnO_2$ to$TiO_2$ ratios of 1:1 and 3:2, respectively. The Ti 2P spectra in Figure 21 (a) and (b) again show three peaks, which are located at 459.2 and 464.9, and 472.6 eV and represent the Ti $2P_{5/2}$, $Ti2P_{3/2}$, and Ti 2P satellite, respectively. The XPS spectra in Figure 21 (b and c) show the presence of Ti in the $TiO_2/SnO_2$ composite fibers, which was present as Ti(VI).

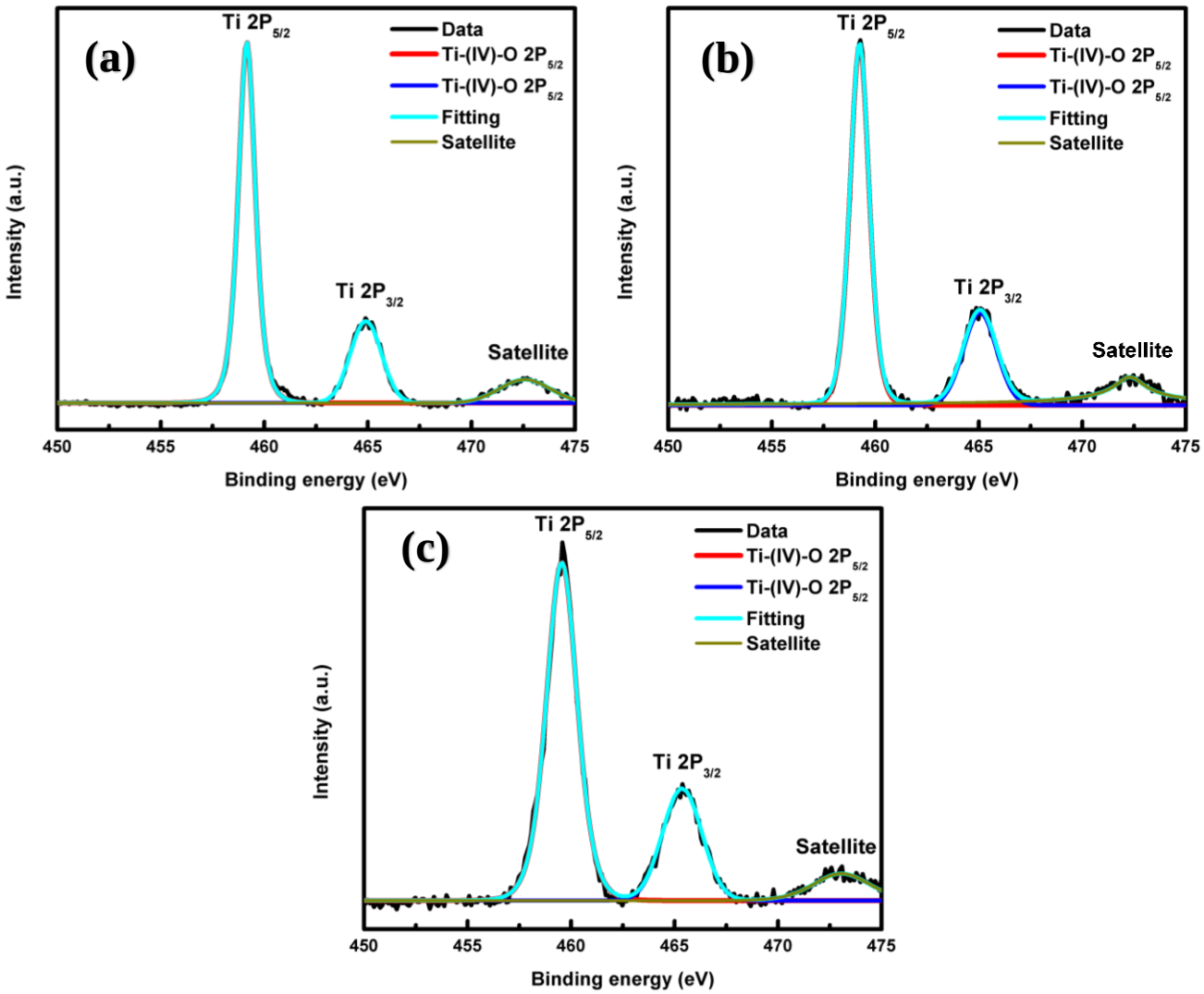


*Figure 21. Ti 2P XPS spectrum of $TiO_2$ oxidized at 700°C (a), $SnO_2$:$TiO_2$ at a ratio of 1:1 (b), and $SnO_2$:$TiO_2$ at a ratio of 3:2 (c).*

Figure 22 (a-d) shows the O 1S XPS spectrum for the as synthesized $SnO_2$, $TiO_2$ and $SnO_2$/$TiO_2$ fibers. Figure 22 (a) shows the spectrum for $SnO_2$ fibers oxidized at 700 °C which was deconvolved into two peaks, which were located at 531 and 532 eV. The two peaks located at 531 and 532 eV are indicative of oxygen bound to a high oxidation state metal such as Sn(IV) and the presence of hydroxide in the sample [88-90]. Figure 22 (b) shows the O1S spectrum for the $TiO_2$ fibers, which was similarly deconvolved into two peaks located at 530 and 532 eV indicating the presence of a high oxidation state metal and the presence of hydroxide. The O1S

spectrum of the $SnO_2/TiO_2$ composite fibers with $SnO_2$ to $TiO_2$ ratios of 1:1 and 3:2 is shown in Figures 22 (c) and 22 (d), respectively. The XPS results for the $SnO_2/TiO_2$ composite fibers showed the presence of two peaks in the O1S spectrum indicating metal-oxygen and the metal-hydroxide bonds, which are located 531 and 532 eV, respectively, as was shown in the in the $TiO_2$ and $SnO_2$ individual samples.

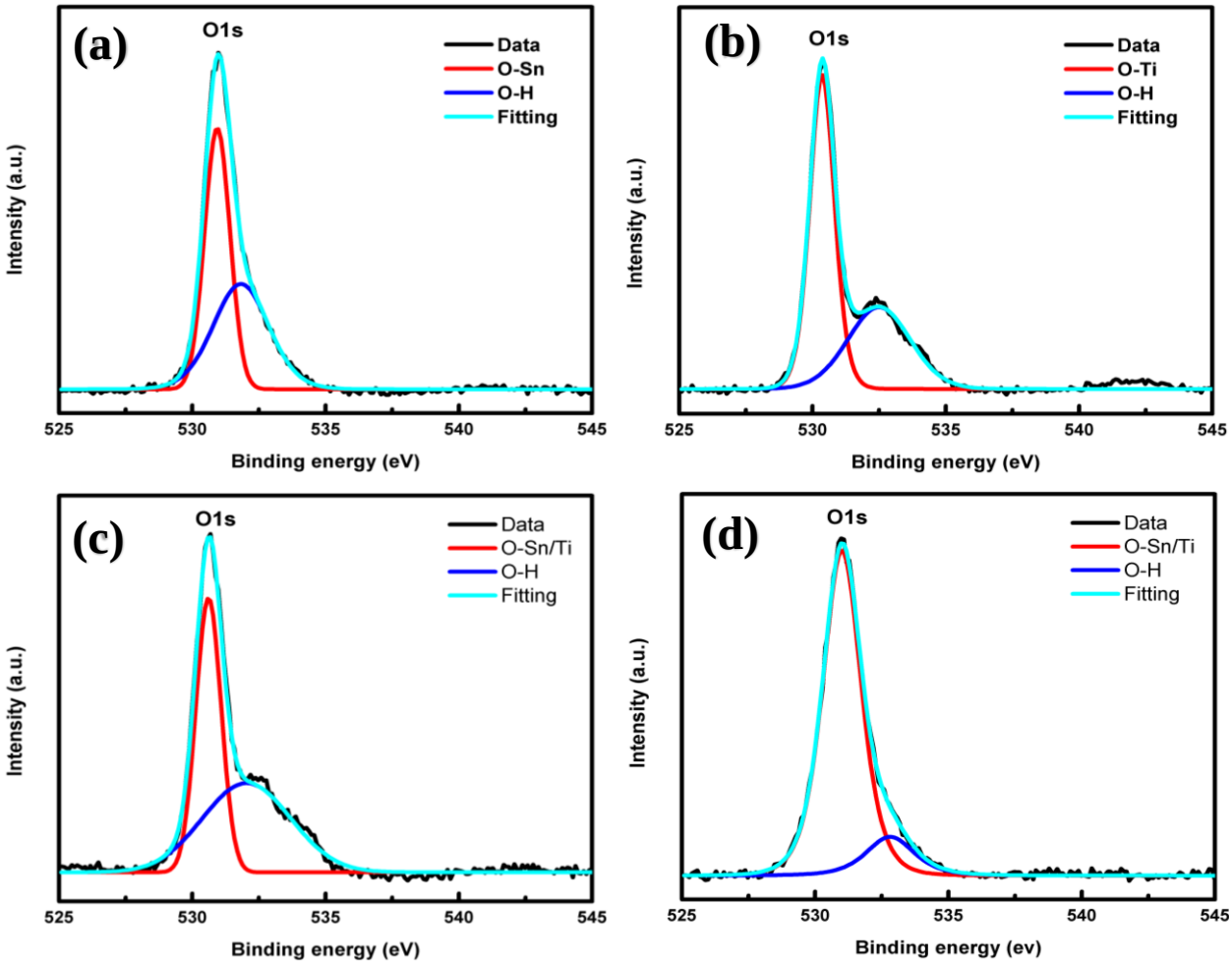


*Figure 22. O1s XPS spectrum of $TiO_2$ oxidized at 700°C (a), $SnO_2$:$TiO_2$ at a ratio of 1:1 (b), and $SnO_2$:$TiO_2$ at a ratio of 3:2 (c).*

### 4.1.2 Ceramic/carbon fiber composites

To study the surface morphology and structure of the carbonized ceramic/carbon composite fibers, SEM images were taken at 5,000 and 15,000 magnification (Figure 23). It can be seen in Figure 23 (a-f) show the SEM images for the ceramic/carbon composite fibers. It can be observed in Figure 23 (a, b) that when the coating with pure $SnO_2$ ceramic fibers, the short-fiber morphology disappeared and instead, spherical particles were embedded on the surface of the FPCFs. In comparison, when using the ceramic composite fibers with 1:1 ($SnO_2$:$TiO_2$) ratio to coat the FPCFs, spherical particles embedded on the surface as well as small nanoflakes on the surrounding can be observed. Similarly, when coating FPCFs with the composite with (3:2) ($SnO_2$:$TiO_2$) ratio, the spherical particles were no longer visible and instead nanoflakes were formed on spherical particles and are deposited on the surface of the FPCFs (Figure 23 (e,f)). Although the short fiber structure was lost, the presence of Sn, Ti, and O is still present within the composite fibers as shown by the EDS spectra of each corresponding sample in figure 24(a-c). Moreover high concentrations of C and N are also observed and can be attributed to the carbonized fibers that were incorporated.

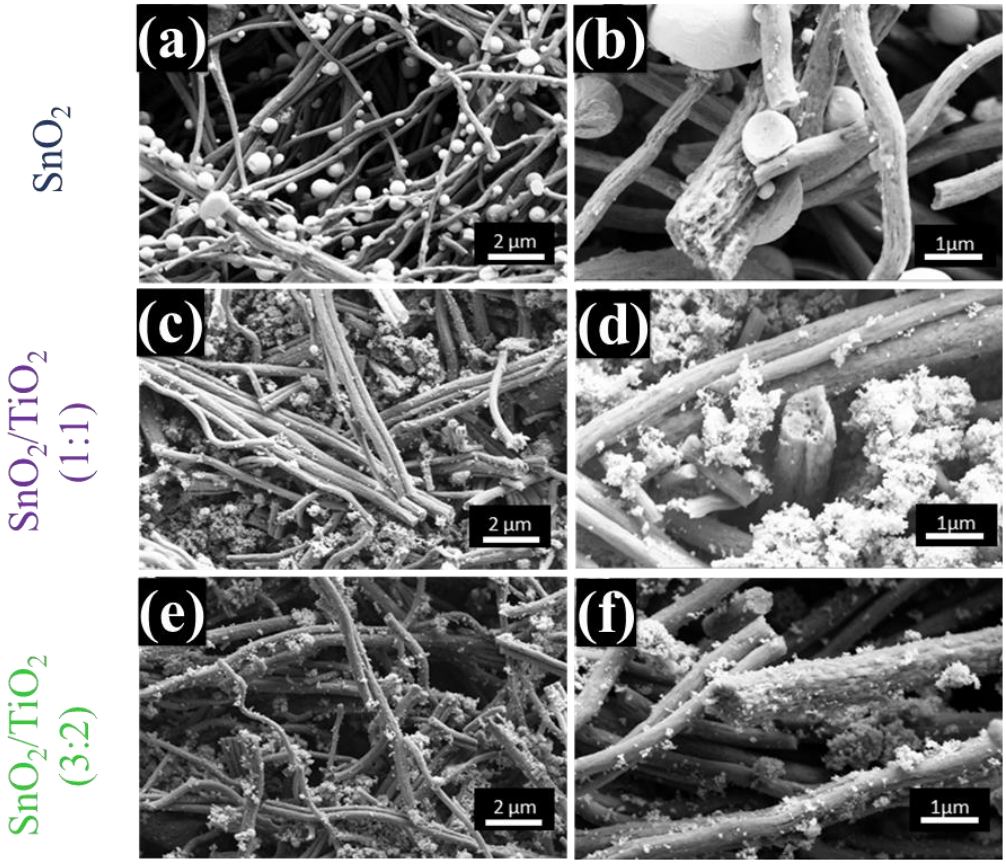


*Figure 23. SEM images of $SnO_2$/FPCFs (a, b), (1:1) $SnO_2$:$TiO_2$ /FPCFs (c, d), (3:2) $SnO_2$:$TiO_2$ /FPCFs (e, f) ceramic/carbon composite fibers at a 5,000 x, 15,000 x magnification.*

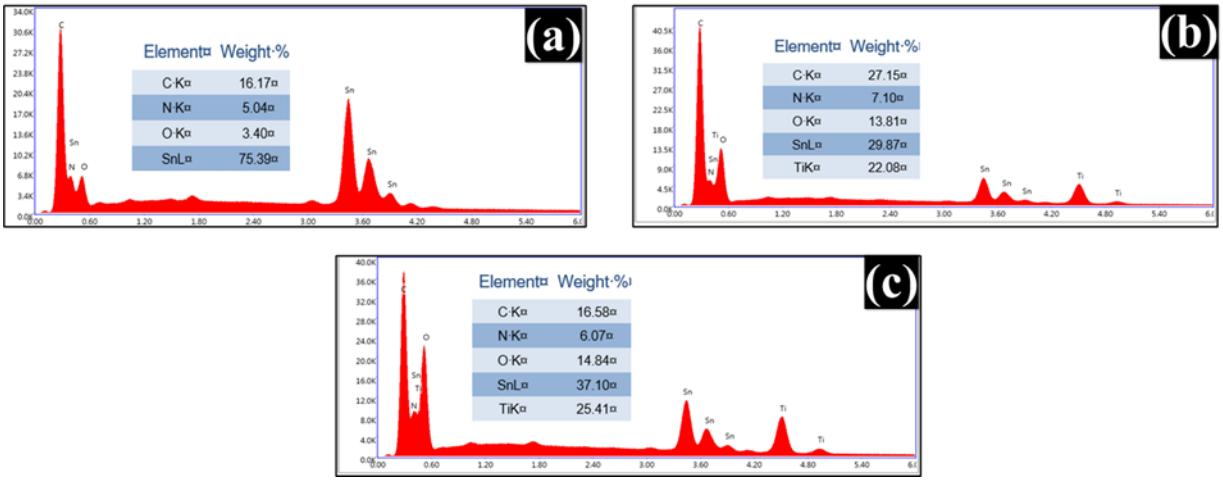


*Figure 24. EDS spectra of $SnO_2$/FPCFs (a), (1:1) $SnO_2$:$TiO_2$ /FPCFs (b), (3:2) $SnO_2$:$TiO_2$ /FPCFs (c) ceramic/carbon composite fibers*

The crystal structure and thermal decomposition of the coated fibers were studied by XRD and TGA, respectively. The diffraction peaks at 35, 38, 50, 53, 65, 74, 75, 77° in 2θ are observed in all the ceramic/carbon samples and are attributed to the presence of metallic Sn, indicating the reduction of $SnO_2$ to Sn after the subsequent heat treatment [27, 31, 91, 92]. Furthermore, the peak at 33° is only present in the $SnO_2$:$TiO_2$ samples and can be assigned to presence of rutile $TiO_2$ within the composites[82, 83, 93]. To investigate the amount of active material retained within the fibers after the carbonization process, TGA experiments (Figure 25b) were performed from 25 to 700 °C at 5 °C/min in air. It is obvious that both, the uncoated and coated FPCFs, exhibit two major-steps losses. The first step loss occurs at 25-250 °C for the FPCFs, at 25-180 °C for the coated FPCFs, and can be attributed to the evaporation of any remaining solvent in the sample. The next step loss can be identified at a temperature range of 440-600 °C for the FPCFs and at 380-500 °C for the coated FPCFs. The residual mass of ~3% for the FPCFs can be attributed to the graphitized residual carbon from the PAN as well as polymer impurities. On the other hand, the residual masses of 52, 53, and 48 % observed for the coated FPCFs represented the amount of $SnO_2$ and $SnO_2$/$TiO_2$ remained in the samples after carbonization.

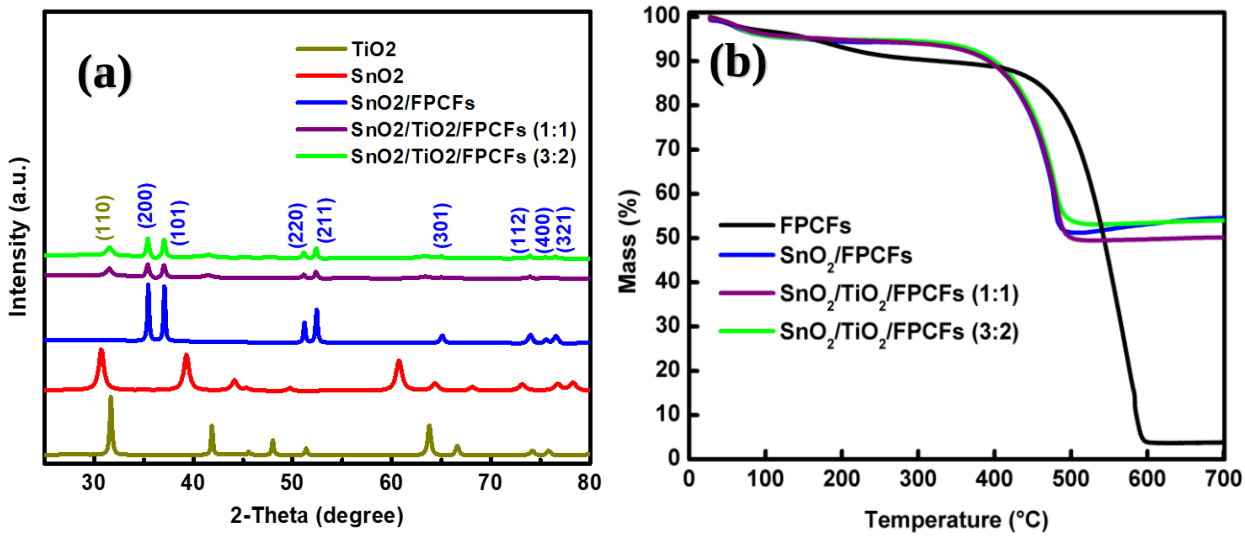


*Figure 25. TGA (a) and XRD (b) of $TiO_2$ (i), $SnO_2$ (ii), ceramic fibers and $SnO_2$/FPCFs (iii), $SnO_2$/TiO2 (1:1)/FPCFs (iv), $SnO_2$/$TiO_2$ (3:2)/FPCFs (v) ceramic/carbon composite fibers.*

X-ray photoelectron (XPS) characterization was conducted to study the composition and chemical states of the synthesized ceramic/carbon composites The XPS survey spectrum for each sample is shown in Figure 26 (a-c), which shows the presence of Sn and O as the major components in the $SnO_2$/FPCFs sample, as well as some carbon and nitrogen attributed to the presence of the carbon fiber matrix. The $SnO_2$/$TiO_2$composite-fiber samples consisted of Ti, Sn and O as well as carbon and nitrogen. Such results confirm the successful coating of the pure ceramic fibers onto the flexible and porous carbon fibers.

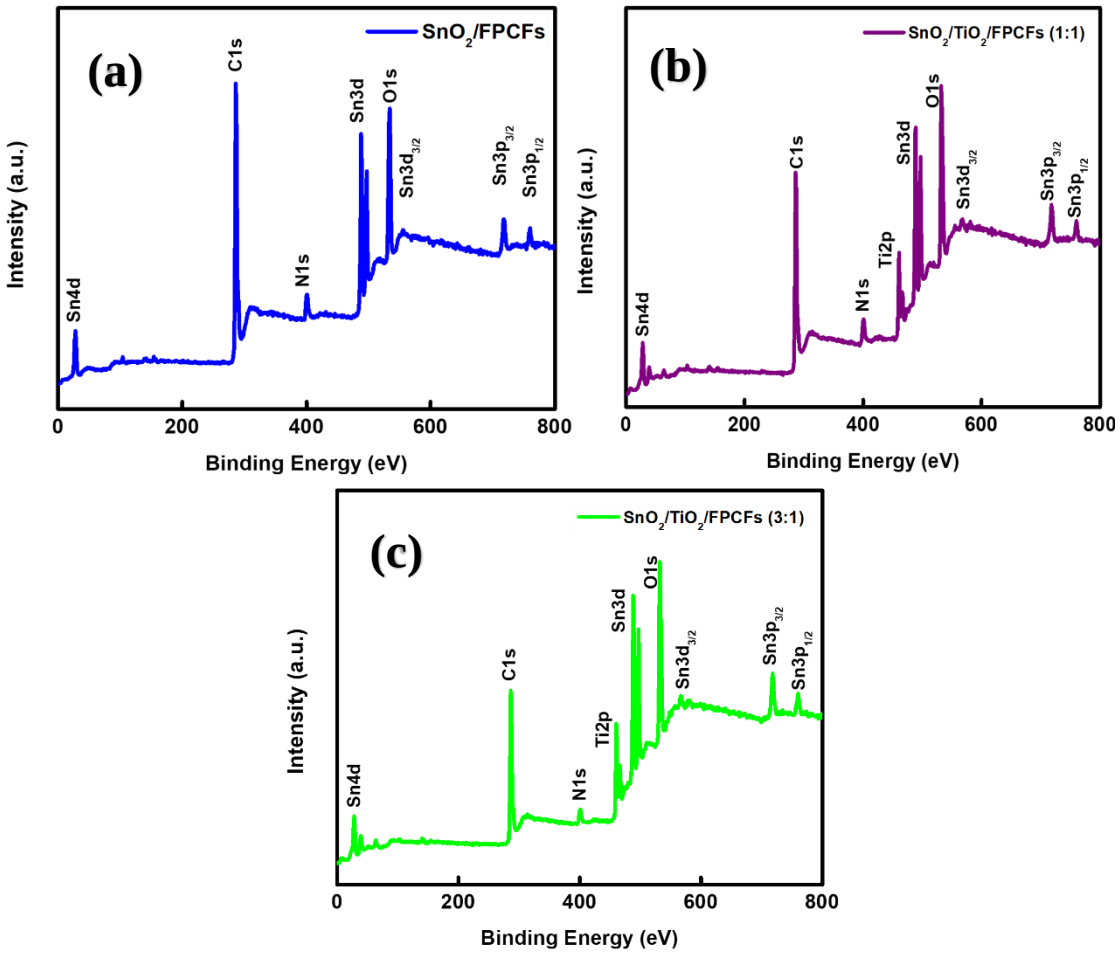


*Figure 26. XPS surveys of $SnO_2$/FPCFs (a), (1:1) $SnO_2$:$TiO_2$ /FPCFs (b), (3:2) $SnO_2$:$TiO_2$ /FPCFs (c) ceramic/carbon composite fibers*

## 4.2 Electrochemical Performance

To study the electrochemical performance of the ceramic/carbon composite fibers various electrochemical analyses were conducted. The cycling capability was studied by galvanostatic charge-discharge testing at a current density of 100 $mAg^{-1}$ over a voltage potential range of 0.05-3.0 V. In addition, the rate performance of the composites was also investigated at different current densities to study the rate capability of the short fibers. Furthermore, cycling voltammetry (CV) experiments were conducted at room temperature to study the redox reactions within the composites and they were performed at a voltage range of 0.01-3 V with a scan rate of 0.02mVs-1 over 4 cycles. The resistance across the cell was also measured conducting electrochemical impedance spectroscopy (EIS).

### 4.2.1 $SnO_2/TiO_2$ ceramic composite fibers

To determine the reduction/oxidation reactions of the anode electrode, CV experiments were performed over a voltage range of 0.05 -3.0 V and at a scan rate of 0.2 $mVs^{-1}$ over four cycles. Figure 27 shows the cyclic voltammetry curves of the $SnO_2/TiO_2$ ceramic composites.

During the first cycle, the peaks at 0.95, 0.11, and the peak between 0.5-1 V can be attributed to the formation of the solid electrolyte interface (SEI), electrolyte decomposition, and the dealloying process generating $Li_xSn$, respectively [33, 94, 95]. Furthermore, the redox peak at 1.3 V is ascribed to the reversible conversion reaction of Sn and $LiO_2$ to form $SnO_2$ while the peak at 1.89 V is attributed to the insertion/ extraction of lithium from $TiO_2$. From the second cycle and beyond, the CV curves coincide with each other, indicating high reversibility and good cycling performance of the anode electrode. The process illustrated by the CV curves can be chemically represented by the following equations [33, 94, 95]:

$$SnO_2 + 4Li^+ + 4e^- \rightarrow Sn + 2Li_2O \qquad (8)$$

$$Sn + xLi^+ + xe^- \leftrightarrow 2Li_xSn\ (0 \leq x \leq 4.4) \qquad (9)$$

$$TiO_2 + xLi^+ + xe^- \leftrightarrow Li_xTiO_2\ (0 \leq x \leq 1) \qquad (10)$$

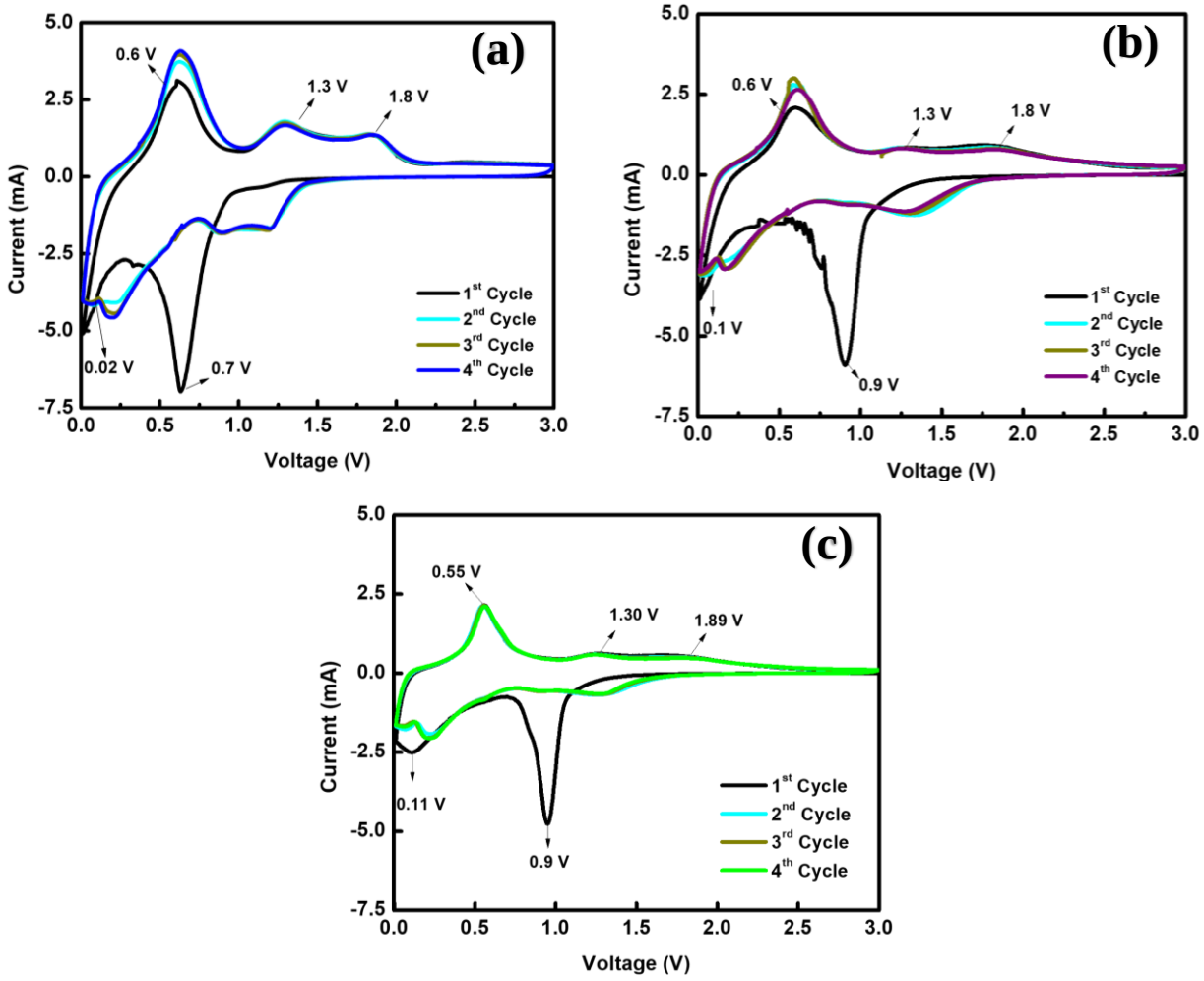


*Figure 27. Cyclic voltammetry of ceramic fibers from $SnO_2$(b), $SnO_2$:$TiO_2$ at a ratio of (1:1) (c) and at a ratio of $SnO_2$:$TiO_2$ at a ratio of (3:2) (d).*

The cycle performance of the $SnO_2/TiO_2$ ceramic fibers was evaluated using galvanostatic experiments at a current density of 100 mA $g^{-1}$ for 70 cycles over a voltage range of 0.05-3.0 V (Figure 28 (a, b) and (c, d), respectively). Initially, the $SnO_2$ ceramic fibers demonstrated irreversible discharge capacity of 1123 mAh $g^{-1}$ and charge capacity of 741 mAh $g^{-1}$; however, the reversible capacity after 70 cycles dropped to 179 mAh $g^{-1}$. Such a capacity reduction has been attributed to the pulverization and instability of $SnO_2$ upon cycling caused by the high-volume change developed during lithium insertion/extraction. In comparison, the SnO2/TiO2 at a (1:1) ratio demonstrated the lowest capacity after 70 cycles. Due to its excessive amount of TiO2 the final capacity resulted in 244 mAh $g^{-1}$. On the other hand, the $SnO_2/TiO_2$ micro-belt fibers (3:2 ratio) demonstrated high but irreversible discharge capacity of 1200 mAh $g^{-1}$ and charge capacity of 820 mAh $g^{-1}$ during the first cycle, resulting in a coulombic efficiency of 65 %. Such irreversible capacity can be attributed to the formation of the SEI at the anode/electrode interface. At the second cycle, the reversible capacity decreased to 700 mAh $g^{-1}$ which was twice than that of graphite; however, after 70 cycles the capacity decreased to 279 mAh $g^{-1}$. Such a drastic drop in capacity can be attributed to inevitable pulverization of the anode upon cycling caused by internal stresses (volume change) during lithiation/de-lithiation. Despite this performance, the electrode retained a high coulombic efficiency of 99% indicating good reversibility. When comparing the pure $SnO_2$ ceramic fibers to the $SnO_2/TiO_2$ composite fibers with a ratio of 1:1 and 3:2 (Fig.28 (a, b)), it was obvious that the $SnO_2/TiO_2$ short fibers demonstrated less volume expansion due to the addition of $TiO_2$ and also to its unique micro-belt structure. Such attributes mitigated the internal stresses experienced upon cycling which resulted in better capacity retention and higher reversible capacity after 70 cycles. More work is needed to improve the electrochemical performance of the $SnO_2/TiO_2$ short-fiber anode.

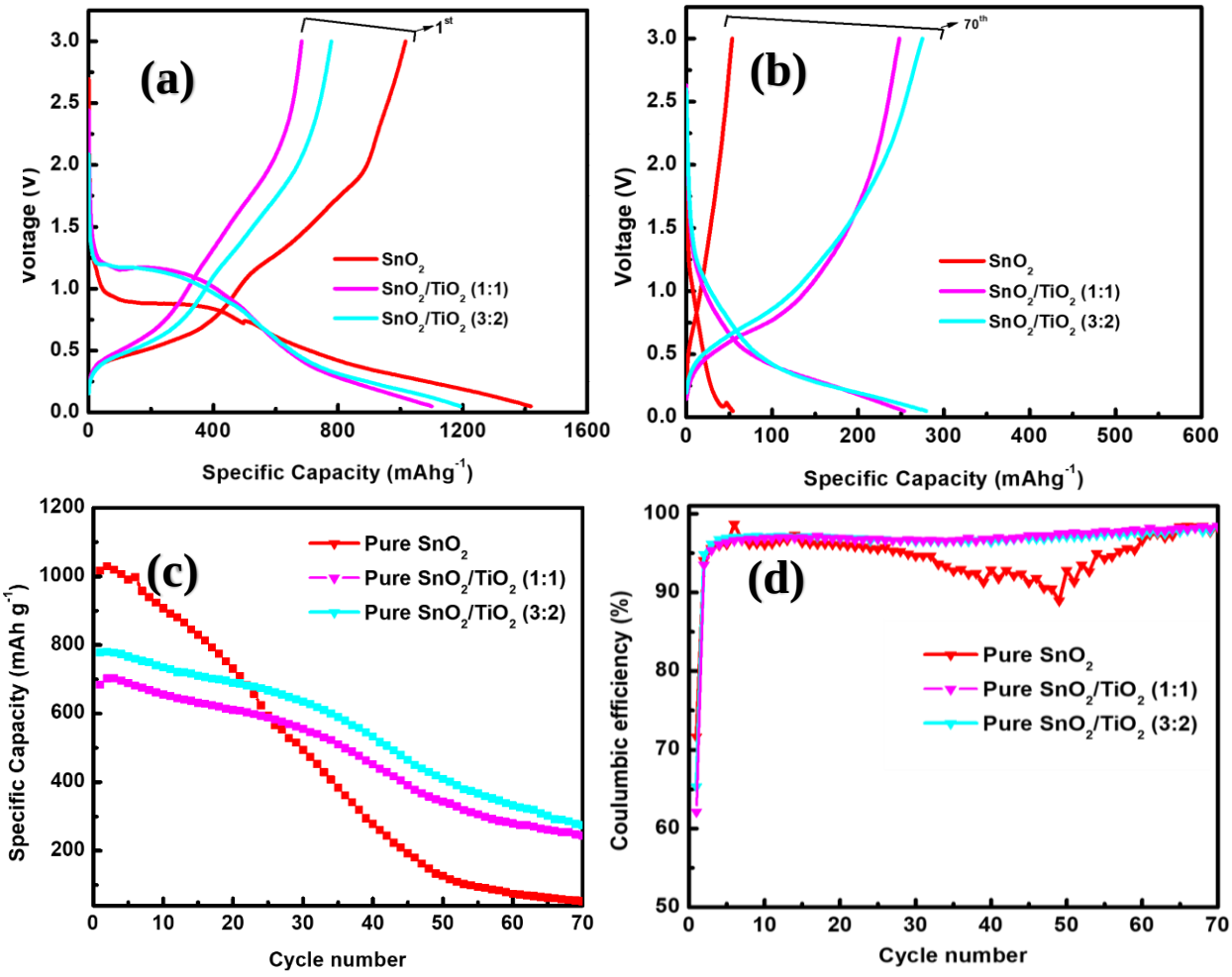


*Figure 28. Charge/discharge curves of the $SnO_2$, (1:1) $SnO_2$:$TiO_2$, (3:2), $SnO_2$:$TiO_2$/FPCFs at the 1st (a) and 100th (b) as well as the charge capacity (c) and coulombic efficiency (d) after 100 cycles at a current density of 100 mA g-1.*

To further investigate the electrochemical performance and reversibility of the composites, the $SnO_2$/$TiO_2$ micro-belt fibers anodes with a ratio of 3:2 were tested at different current rates (the rate performance results are shown in figure 29. It can be observed that the $SnO_2$/$TiO_2$ micro-belt fibers delivered a high initial capacity of 723 at 50 mAh g-1 attributed to its high content of $SnO_2$ which yields high capacities. Moreover when the current density reached 500 mA $g^{-1}$, the micro-belt fibers retained a capacity of 250 mAh $g^{-1}$ accredited to the addition of $TiO_2$ that serves a buffer for volume expansion. However, when the current rate is brought back to 50 mA $g^{-1}$ the composite returns a capacity of only 470 mAhg-1, indicating a

poor reversibility. Such results can be attributed to its brittle properties that cause the material to pulverize over prolonged cycling.

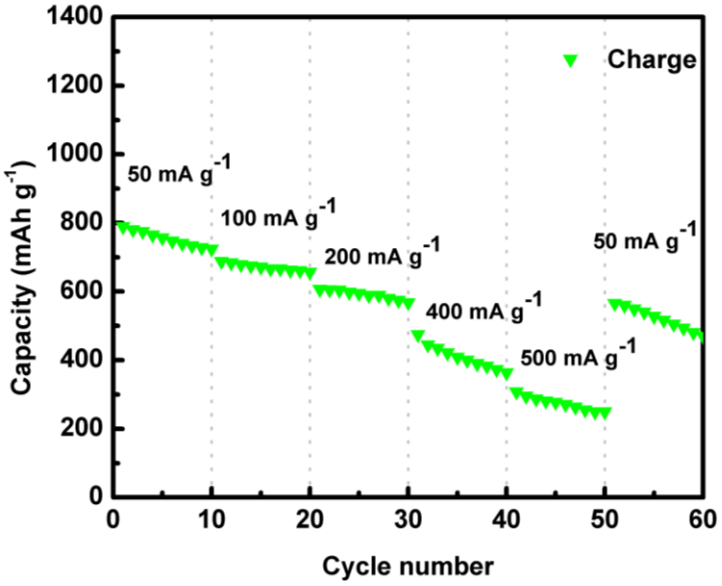


*Figure 29. Rate performance of SnO2/TiO2 short-fiber (3:2 ratio) anode.*

**4.2.2 Ceramic/carbon fiber composites**

To study the lithiation/delithiation reactions of the anodes, CV tests were performed for 4 cycles over a voltage potential window of 0.05- 3 V and a scan rate of 0.2 $mVs^{-1}$. Figure 30 shows the CV curves for the $SnO_2$:$TiO_2$/FPCFs composites. During the first cycle, three main reduction peaks are visible at 1, 0.7, and 0.3 V. These peaks represent the breakdown of electrolyte, the SEI layer formation, and the alloying reaction between Li and Sn, respectively. Additionally, the oxidation peaks at 0.65, 0.75, 0.8 V are ascribed to the dealloying of LixSn, while the broad peak at 1.2 V represents the extraction of lithium from the carbon and overlaps with the peak at 1.3 V that corresponds to the insertion/extraction of lithium from titanium. [25, 26, 28, 92, 96, 97]. Moreover, Equation 11 represents the irreversible reaction of $SnO_2$ with $LiO_2$ to form LixSn, which contributes to the first irreversible capacity. Equation 12 is ascribed to the reversible capacity that results from the alloying/dealloying of Sn and Li. Equation 13 illustrates

the insertion/extraction reaction which is attributed to the interaction between lithium and $TiO_2$ while Equation 14 represents the interaction between Li and the carbon fibers. After the first cycle, the CV curves overlap each other, indicating good capacity reversibility of the $SnO_2$:$TiO_2$/FPCFs composite anode.

$$SnO_2 + 4Li^+ + 4e^- \rightarrow Sn + 2Li_2O \quad (11)$$

$$Sn + xLi^+ + xe^- \leftrightarrow 2Li_xSn \ (0 \leq x \leq 4.4) \quad (12)$$

$$TiO_2 + xLi^+ + xe^- \leftrightarrow Li_xTiO_2 \ (0 \leq x \leq 1) \quad (13)$$

$$6C + xLi^+ + xe^- \leftrightarrow Li_xC_6 \ (0 \leq x \leq 1) \quad (14)$$

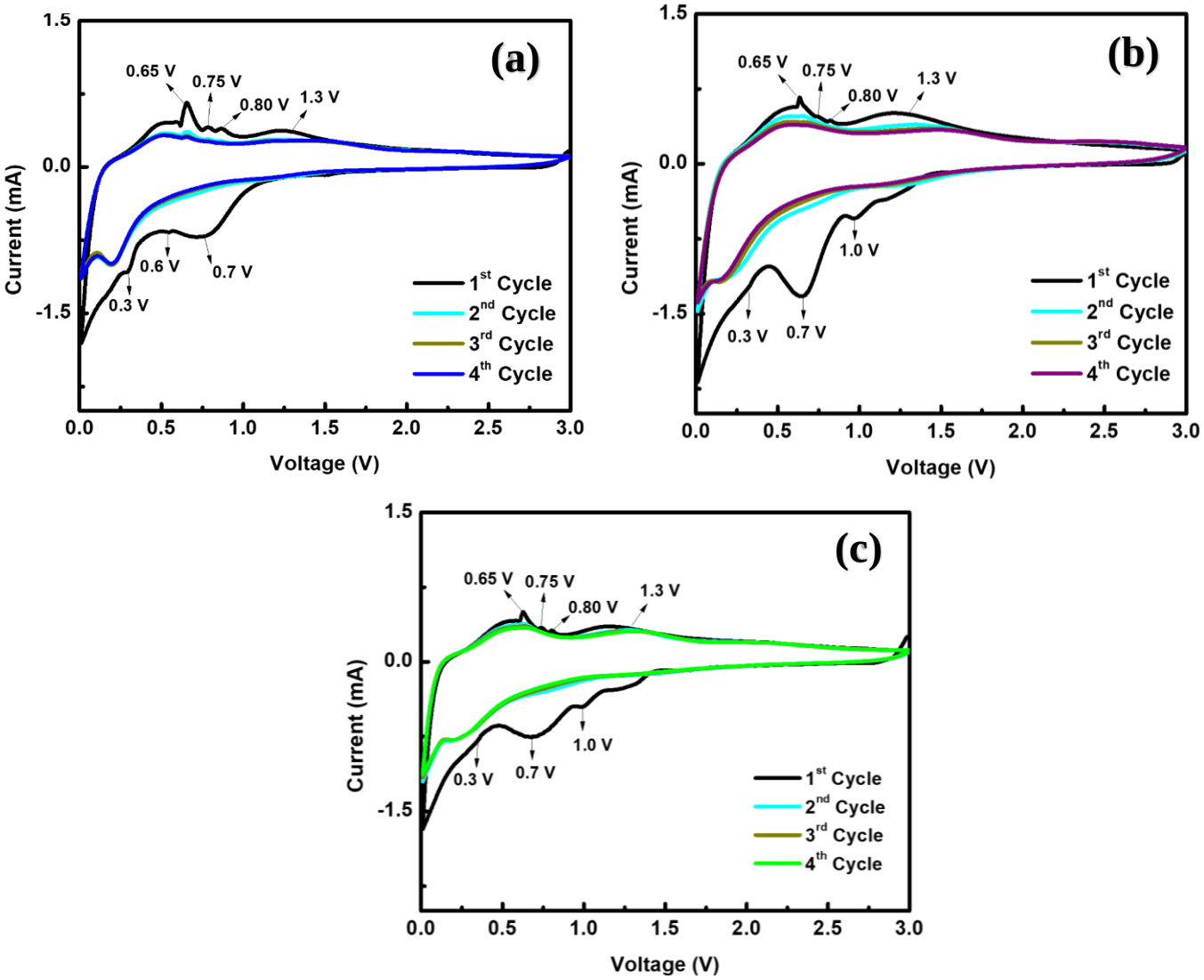


*Figure 30. CV curves of $SnO_2$/FPCFs (a, b,), (1:1) $SnO_2$:$TiO_2$ /FPCFs (c, d), (3:2) $SnO_2$:$TiO_2$ /FPCFs (e, f) ceramic/carbon composite fibers*

To investigate the electrochemical performance of the $SnO_2$/FPCFs, (1:1) $SnO_2$:$TiO_2$/FPCFs, and (3:2) $SnO_2$:$TiO_2$/FPCFs, galvanostatic charge/discharge experiments were performed at a current density of 100 mA $g^{-1}$ from 0.05-3.0V for 100 cycles. Figures 31 (a, b) show the cycling performance of the ceramic/carbon composite fibers after the 1st and 100th cycle. At the 1st cycle, the $SnO_2$/FPCFs, (1:1) $SnO_2$:$TiO_2$/FPCFs, and (3:2) $SnO_2$:$TiO_2$/FPCFs delivered a discharge capacity of 1903, 1920, and 1839 mAh $g^{-1}$, respectively. Such large

capacities can be accredited to the high theoretical capacity of $Sn/SnO_2$ as well as the large number of Li-ions intercalated with carbon in the porous carbon-fiber matrix during the first cycle. However, such high capacities are also irreversible due to the formation of the SEI layer that takes a substantial amount of Li-ions as it forms on the anode surface. For this reason, the charge capacity of ceramic/carbon composite fibers decreased to 1290,1240, and 1197 mAh $g^{-1}$, resulting in a low coulombic efficiency of 67, 64, and 65 %, for the $SnO_2$ /FPCFs, (1:1) $SnO_2$:$TiO_2$/FPCFs, and the (3:2) $SnO_2$:$TiO_2$/FPCFs, respectively (Figure 31 d). However, after the second cycle, the coulombic efficiency increases to 98 % for all ceramic/carbon composites and remains stable, indicating good reversibility of the porous carbon fibers. After 100 cycles, the (3:2) $SnO_2$:$TiO_2$/FPCFs delivered a reversible capacity of 890 mAh $g^{-1}$ while the $SnO_2$ and (1:1) $SnO_2$:$TiO_2$/FPCFs anodes exhibited a capacity of 877, and 840 mAh $g^{-1}$, respectively. As shown in Figure 31 (c), though the capacity of the (3:2) $SnO_2$:$TiO_2$/FPCFs composite was slightly higher, the overall cycling stability demonstrated by this composite was better than that of the $SnO_2$/FPCFs and the (1:1) $SnO_2$:$TiO_2$/FPCFs, which is which is due to the synergetic effect of $TiO_2$ achieved in this study.

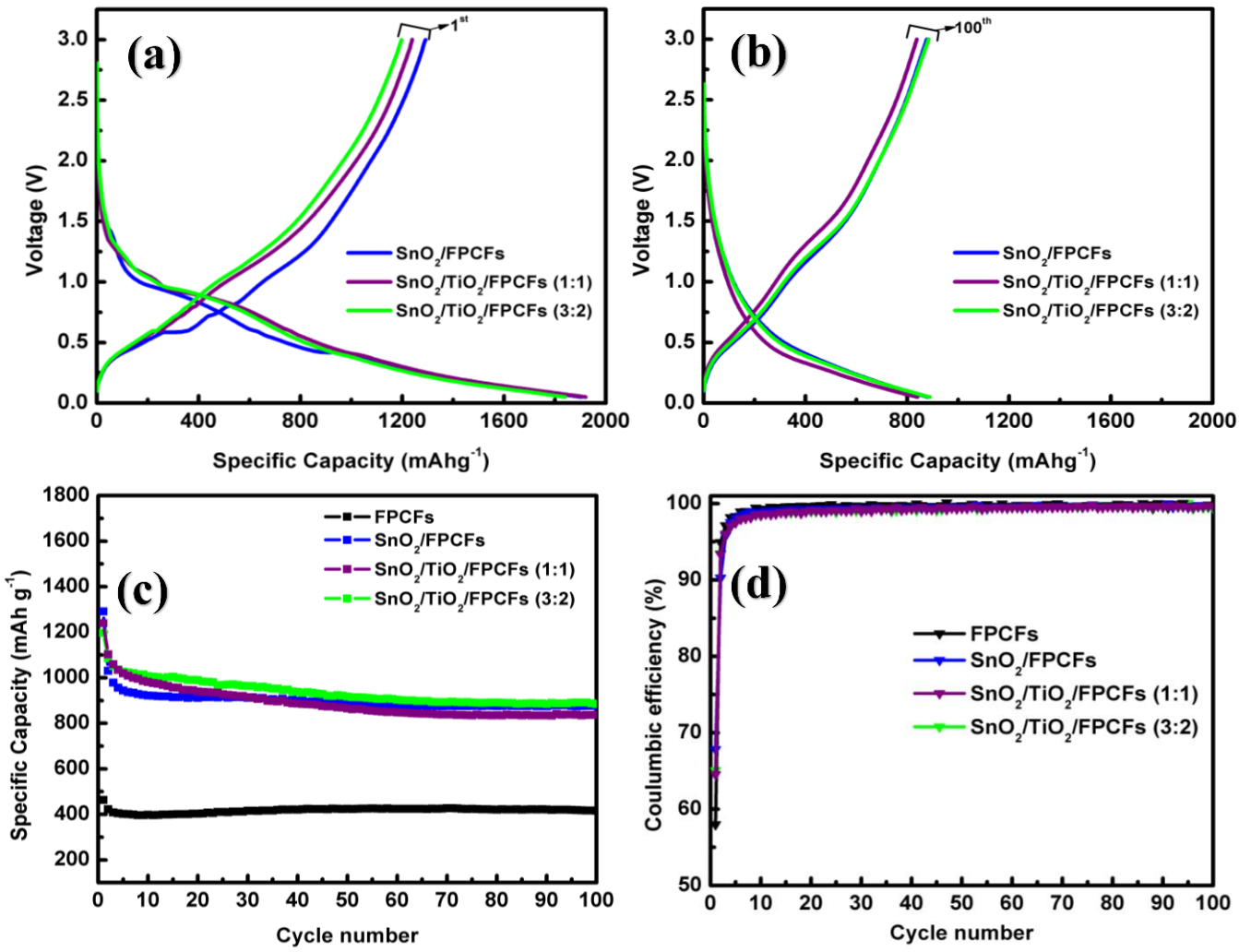


*Figure 31. Charge/discharge curves of the $SnO_2$/FPCFs, (1:1) $SnO_2$:$TiO_2$ /FPCFs, (3:2) $SnO_2$:$TiO_2$ /FPCFs at the 1st (a) and 100th (b) as well as the charge capacity (c) and coulombic efficiency (d) after 100 cycles at a current density of 100 mA $g^{-1}$.*

Furthermore, to gain more insight on the cycling performance of the ceramic/carbon composites, charge/discharge cycles were also carried at 200 mA $g^{-1}$ for 100 cycles over a potential of 0.05-3.0V. As expected, it can be observed in Figure 32 (a, b) that the fibers coated with $SnO_2$:$TiO_2$/FPCFs demonstrated better cycling stability when compared to that of the $SnO_2$/FPCFs, which is due to the addition of $TiO_2$ which reduced the capacity loss at the first 20 cycles. At the first cycle, the $SnO_2$/FPCFs demonstrated a higher charge capacity of 636 mAh $g^{-1}$ when compared to that of the (1:1) $SnO_2$:$TiO_2$)FPCFs and (3:2) $SnO_2$:$TiO_2$/FPCFs which delivered a charge capacity of 568, and 591 mAh $g^{-1}$, respectively. The lower capacity delivered by the (1:1) $SnO_2$:$TiO_2$/FPCFs was caused by the addition of $TiO_2$ which hindered the overall lithium storage of the composite due to its low theoretical capacity. However, after 100 cycles, the (3:2) $SnO_2$:$TiO_2$/FPCFs retained a larger capacity of 420 mAh $g^{-1}$ while the $SnO_2$ and the (1:1) $SnO_2$:$TiO_2$/FPCFs ratio only yielded a capacity of 369 and 370 mAh $g^{-1}$, respectively. The improved electrochemical performance of the (3:2) $SnO_2$:$TiO_2$/FPCFs can once again be attributed to the contribution of $TiO_2$ which can mitigate the large volume expansion of $SnO_2$ during lithiation/delithiation, improving the capacity retention and also the overall cycling stability.

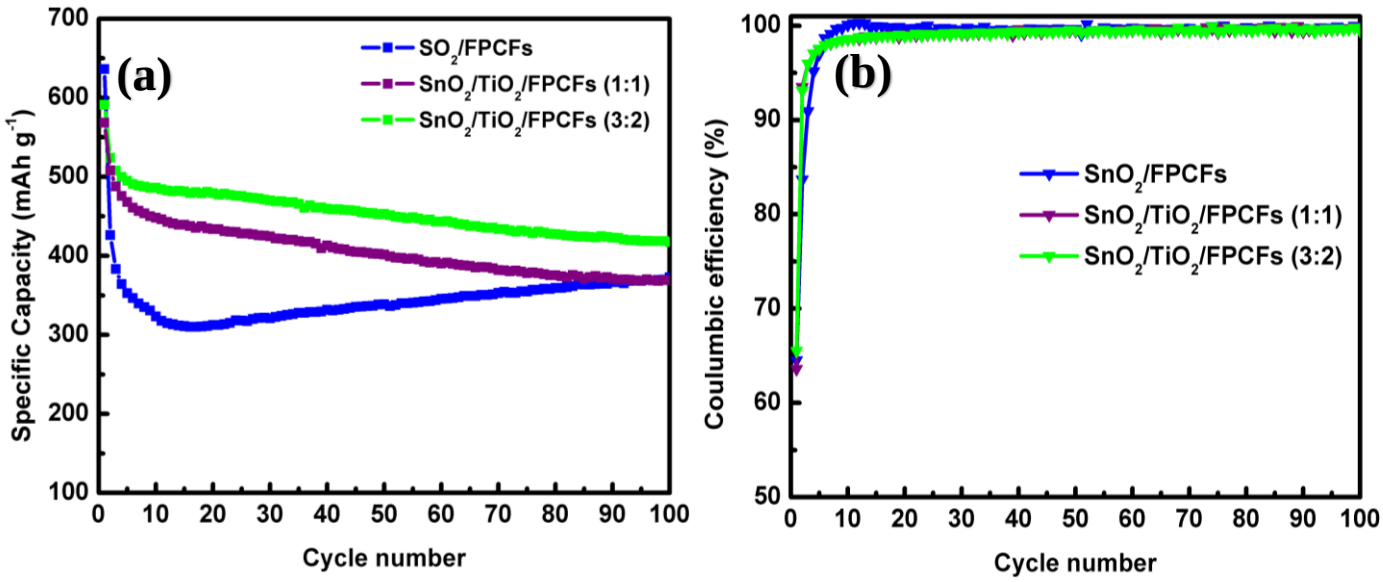


*Figure 32. Charge profiles (a) and coulombic efficiency (b) of the $SnO_2$/FPCFs, (1:1) $SnO_2$:$TiO_2$ /FPCFs, and (3:2) $SnO_2$:$TiO_2$/FPCFs ceramic/carbon composite fibers after 100 cycles at a current density of 200 mA $g^{-1}$.*

To investigate the rate capability of the ceramic/carbon composites, charge/discharge experiments were performed at 50, 100, 200, 400, 500, and back at 50 mA $g^{-1}$ for 10 cycles. It can be seen in figure 33 that the fibers coated with (3:2) $SnO_2$:$TiO_2$ outperformed all the other composites. When the current density was increased to 500 mAh $g^{-1}$, the (3:2) $SnO_2$:$TiO_2$/FPCFs retained a capacity of 323 mAh $g^{-1}$ while the $SnO_2$/FPCFs and the pure FPCFs showed a capacity of 210 and 130 mAh $g^{-1}$, respectively. In contrast, the (1:1) $SnO_2$:$TiO_2$/FPCFs yielded the lowest capacity which was 39 mAh $g^{-1}$ which was caused by the excessive addition of $TiO_2$ that lowered the capacity of the overall composite. When the current density was brought back to 50 mA $g^{-1}$, the (3:2) $SnO_2$:$TiO_2$/FPCFs delivered a capacity of 908 mAh $g^{-1}$,. while he pristine FPCFs yielded a capacity of 758, 727, and 424 mAh $g^{-1}$, at respectively. Most importantly, the (3:2) $SnO_2$:$TiO_2$/FPCFs demonstrated a 100% reversibility and the highest capacity achieved when compared to that of the $SnO_2$/FPCFs, (1:1) $SnO_2$:$TiO_2$/FPCFs which makes this composite a material of interest for use as an anode material in LIBs.

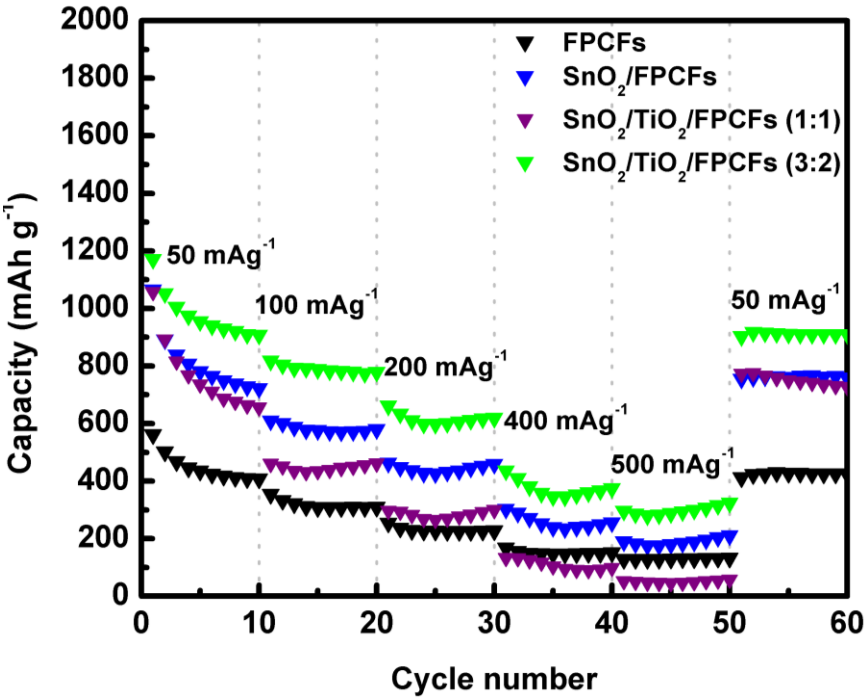


*Figure 33. Rate performance of the $SnO_2$/FPCFs, (1:1) $SnO_2$:$TiO_2$/FPCFs, and (3:2) $SnO_2$:$TiO_2$/FPCFs ceramic/carbon composite fibers at different current densities.*

To further study and analyze the electrochemical properties and kinetics of the as-prepared anodes, electrochemical impedance spectroscopy (EIS) measurements were performed at an open circuit voltage and the results are shown in Figure 34. The Nyquist plots in Figure 34 (a) can be divided into two sections which are the semicircle located at the high-medium frequencies and the slope line in the low frequency range. The semicircle can be ascribed to the diffusion of Li-ions through the SEI layer and the charge transfer resistance at the electrode-electrolyte interface. Next, the slanted slope line at the low frequencies is assigned to the diffusion of Li ions through the active material. The EIS results were analyzed and fitted by the equivalent circuit illustrated in Figure 34 (b). In this circuit, Rs, Rct, W, and CPE represent the electrolyte solution resistance, the charge transfer resistance, the Warburg impedance, and the phase-angle element that is equivalent to the double layer capacitance, respectively. Based on Nyquist plots shown in Figure 34 (a), the FPCFs, $SnO_2$/FPCFs, (1:1) $SnO_2$:$TiO_2$/FPCFs, and

**(**3:2) $SnO_2$:TiO /FPCFs, demonstrated an overall resistance of 500,430, 570, and 370 Ω, respectively. The improved resistance of the (3:2) $SnO_2$:$TiO_2$/FPCFs can be attributed to the heterojunction formed between Sn, $SnO_2$ and $TiO_2$ as well as the synergistic effect of the particles within the flexible porous matrix which resulted in improved Li transport and lower charge transfer resistance when compared to the other composite electrodes [33].

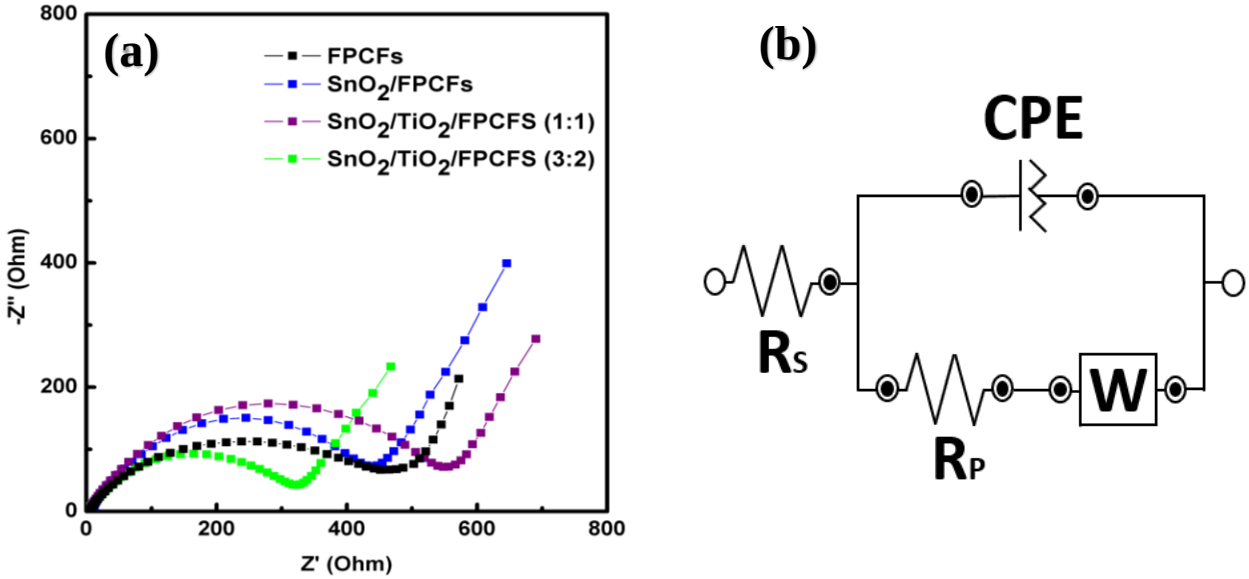


*Figure 34. Nyquist impedance (a) of the $SnO_2$/FPCFs, (1:1) $SnO_2$:$TiO_2$/FPCFs, and (3:2) $SnO_2$:$TiO_2$/FPCFs ceramic/carbon composite fibers before cycling and the equivalent circuit (b)*

.

# CHAPTER V

# CONCLUSION

Short $SnO_2$:$TiO_2$ micro belt-fibers were successfully synthesized through safe, facile, and fast processing fiber production method. The short micro-belt fibers were synthesized using tin and titanium precursors mixed in ethanol/PVP, which was used in the centrifugal spinning process. The calcination of the precursor fibers in air at 700 °C resulted in a short micro belt-fiber morphology with spherical particles on the surface which was observed by the SEM studies. Furthermore, the phases, stability, and elemental composition of $SnO_2$:$TiO_2$ were confirmed using EDS, XPS, and TGA analysis. The XRD patterns confirmed the presence of crystal structure of $SnO_2$ and the rutile phase of $TiO_2$ within the fibers. In addition, when used as an anode material in LIBs, the $SnO_2$:$TiO_2$ micro belt-fibers demonstrated initial irreversible capacity of 1200 mAh $g^{-1}$ and reversible charge capacity of 820 mAh $g^{-1}$ when tested at a current rate of 100 mA $g^{-1}$. However, due to the pulverization of the anode upon cycling, the reversible capacity decreased to 279 mAh $g^{-1}$ after 70 cycles. Additionally, the $SnO_2$ and $SnO_2$:$TiO_2$ composite fibers were successfully coated onto centrifugally spun PAN/PMMA fibrous mats which yielded ceramic/carbon composite fibers after a subsequent heat treatment. The surface morphology and structure of the as-prepared composite fibers was investigated by SEM which confirmed that the particles were successfully attached to the surface of the carbon porous fibers. The presence, phases, and crystal structure of metallic Sn, $SnO_2$ as well as $TiO_2$

within the carbon composite fibers was confirmed by EDS, XPS and TGA, respectively. Moreover, when used as a binder-free anode in LIBs, the (3:2) $SnO_2$:$TiO_2$/FPCFs delivered a high reversible capacity of 890 mAh $g^{-1}$ after 100 cycles at 100 mA $g^{-1}$. More interestingly, when tested at a high current density of 200 mA $g^{-1}$, the composite-fiber anode delivered a capacity of 419 mAh $g^{-1}$ after 100 cycles and coulombic efficiency of 99 % after the $2^{nd}$ cycle up to the $100^{th}$ cycle, indicating good cyclic stability and performance. In addition, when tested at different current densities, the (3:2) $SnO_2$:$TiO_2$/FPCFs initially delivered a capacity of 1171 mAh $g^{-1}$ at 50 mA $g^{-1}$ and retained a capacity of 323 mAh $g^{-1}$ at high current rate of 500 mA $g^{-1}$. After the current density was lowered back to 50 mA $g^{-1}$, the (3:2) $SnO_2$:$TiO_2$/FPCFs delivered a capacity of 908 mAh $g^{-1}$, depicting great rate capabilities. The overall electrochemical performance demonstrated by the ceramic/carbon composite shows a great potential for use as anode in LIBs.

.

# CHAPTER VI

# FUTURE WORK

For future work it is important to improve the subsequent treatment of both the pure ceramic fibers and the ceramic/carbon fiber composites. This may help retain the structure of the $SnO_2$ and $SnO_2$:$TiO_2$ ceramic fibers when being coated onto the FPCFs. Moreover, by improving the subsequent heat treatment, the reduction of $SnO_2$ to metallic Sn can also be avoided. Furthermore, the percentage of pure ceramic fibers being coated onto the FPCFs can also be optimized to achieve better particle distribution after the heat treatment and enhance the electrochemical performance.

REFERENCES


1. Chen, K.-H., et al., *Efficient fast-charging of lithium-ion batteries enabled by laser-patterned three-dimensional graphite anode architectures.* Journal of Power Sources, 2020. **471**: p. 228475.
2. Kim, J., S.M.N. Jeghan, and G. Lee, *Superior fast-charging capability of graphite anode via facile surface treatment for lithium-ion batteries.* Microporous and Mesoporous Materials, 2020. **305**: p. 110325.
3. Roy, P. and S.K. Srivastava, *Nanostructured anode materials for lithium ion batteries.* Journal of Materials Chemistry A, 2015. **3**(6): p. 2454-2484.
4. Wang, Q., et al., *A review of lithium ion battery failure mechanisms and fire prevention strategies.* Progress in Energy and Combustion Science, 2019. **73**: p. 95-131.
5. Goriparti, S., et al., *Review on recent progress of nanostructured anode materials for Li-ion batteries.* Journal of power sources, 2014. **257**: p. 421-443.
6. Yaroslavtsev, A.B. and I.A. Stenina, *Carbon coating of electrode materials for lithium-ion batteries.* Surface Innovations, 2020: p. 1-19.
7. Jung, J.-W., et al., *Electrospun nanofibers as a platform for advanced secondary batteries: a comprehensive review.* Journal of materials chemistry A, 2016. **4**(3): p. 703-750.
8. Ji, L., et al., *Graphene-Based Nanocomposites for Energy Storage.* Advanced Energy Materials, 2016. **6**(16): p. 1502159.

9. Wang, Q., et al., *Thermal runaway caused fire and explosion of lithium ion battery.* Journal of power sources, 2012. **208**: p. 210-224.

10. Lu, J., et al., *The role of nanotechnology in the development of battery materials for electric vehicles.* Nature nanotechnology, 2016. **11**(12): p. 1031.

11. Pampal, E.S., et al., *A review of nanofibrous structures in lithium ion batteries.* Journal of Power Sources, 2015. **300**: p. 199-215.

12. Chen, K., M. Pi, and D. Zhang, *Ultraviolet irradiation enhanced formaldehyde-sensing performance based on SnO2@ TiO2 nanofiber heteroarchitectures.* Journal of Physics D: Applied Physics, 2020. **53**(12): p. 125301.

13. Tan, W.K., et al., *Nanomaterial Fabrication through the Modification of Sol–Gel Derived Coatings.* Nanomaterials, 2021. **11**(1): p. 181.

14. Ślosarczyk, A., *Carbon Fiber—Silica Aerogel Composite with Enhanced Structural and Mechanical Properties Based on Water Glass and Ambient Pressure Drying.* Nanomaterials, 2021. **11**(2): p. 258.

15. Pelzer, M., et al., *Melt spinning and characterization of hollow fibers from poly (4-methyl-1-pentene).* Journal of Applied Polymer Science, 2021. **138**(1): p. 49630.

16. Ji, L., et al., *Recent developments in nanostructured anode materials for rechargeable lithium-ion batteries.* Energy & Environmental Science, 2011. **4**(8): p. 2682-2699.

17. Reddy, M., G. Subba Rao, and B. Chowdari, *Metal oxides and oxysalts as anode materials for Li ion batteries.* Chemical reviews, 2013. **113**(7): p. 5364-5457.18. Akia, M., K.A. Mkhoyan, and K. Lozano, *Synthesis of multiwall α-Fe2O3 hollow fibers via a centrifugal spinning technique.* Materials Science and Engineering: C, 2019. **102**: p. 552-557.

19. Li, Z., et al., *Tin/tin antimonide alloy nanoparticles embedded in electrospun porous carbon fibers as anode materials for lithium-ion batteries.* Journal of Materials Science, 2019. **54**(12): p. 9025-9033.

20. Li, Q., et al., *Extra storage capacity in transition metal oxide lithium-ion batteries revealed by in situ magnetometry.* Nature Materials, 2021. **20**(1): p. 76-83.

21. Reddy, R.C.K., et al., *Progress of nanostructured metal oxides derived from metal–organic frameworks as anode materials for lithium–ion batteries.* Coordination Chemistry Reviews, 2020. **420**: p. 213434.

22. Tian, Q., et al., *The sandwiched buffer zone enables porous SnO2@ C micro-/nanospheres to toward high-performance lithium-ion battery anodes.* Electrochimica Acta, 2020. **354**: p. 136699.

23. Luo, J., et al., *Rationally designed hierarchical TiO2@ Fe2O3 hollow nanostructures for improved lithium ion storage.* Advanced Energy Materials, 2013. **3**(6): p. 737-743.

24. Sun, Y.-N., et al., *Ultrafine SnO2 nanoparticles anchored on N, P-doped porous carbon as anodes for high performance lithium-ion and sodium-ion batteries.* Journal of colloid and interface science, 2020. **572**: p. 122-132.

25. Lin, Z., et al., *Convenient fabrication of a core–shell Sn@ TiO 2 anode for lithium storage from tinplate electroplating sludge.* Chemical Communications, 2020. **56**(70): p. 10187-10190.

26. Hassan, F.M., et al., *Sn/SnO2 embedded in mesoporous carbon nanocomposites as negative electrode for lithium ion batteries.* Electrochimica Acta, 2013. **87**: p. 844-852.

27. Liao, J.Y. and A. Manthiram, *Mesoporous TiO2-Sn/C Core-Shell Nanowire Arrays as High-Performance 3D Anodes for Li-Ion Batteries.* Advanced Energy Materials, 2014. **4**(14): p. 1400403.

28. Yang, Z., et al., *Tin nanoparticles encapsulated carbon nanoboxes as high-performance anode for lithium-ion batteries.* Frontiers in chemistry, 2018. **6**: p. 533.

29. Ding, Y., et al., *Design of multishell microsphere of transition metal oxides/carbon composites for lithium ion battery.* Chemical Engineering Journal, 2020. **380**: p. 122489.

30. Liu, M., et al., *A general strategy to construct yolk-shelled metal oxides inside carbon nanocages for high-stable lithium-ion battery anodes.* Nano Energy, 2020. **68**: p. 104368.

31. Ryu, J., et al., *Dual Buffering Inverse Design of Three-Dimensional Graphene-Supported Sn-TiO2 Anodes for Durable Lithium-Ion Batteries.* Small, 2020. **16**(46): p. 2004861.

32. Sun, L., et al., *Design of Double-shelled TiO2@ SnO2 Nanotubes via Atomic Layer Deposition for Improved Lithium Storage.* CrystEngComm, 2021.

33. Li, R., et al., *Sphere-like SnO2/TiO2 composites as high-performance anodes for lithium ion batteries.* Ceramics International, 2019. **45**(10): p. 13530-13535.

34. Akurati, K.K., et al., *One-step flame synthesis of SnO2/TiO2 composite nanoparticles for photocatalytic applications.* International Journal of Photoenergy, 2005. **7**.

35. Chen, J.S. and X.W. Lou, *SnO2-based nanomaterials: synthesis and application in lithium-ion batteries.* small, 2013. **9**(11): p. 1877-1893.

36. Shi, H., et al., *Highly porous SnO2/TiO2 electrospun nanofibers with high photocatalytic activities.* Ceramics International, 2014. **40**(7): p. 10383-10393.

37. Aravindan, V., et al., *Does carbon coating really improves the electrochemical performance of electrospun SnO2 anodes?* Electrochimica Acta, 2014. **121**: p. 109-115.

38. Bao, D. and Q. Tian, *Interconnected quasi-nanospheres of SnO2/TiO2/C with gap spaces for improved lithium storage.* Materials Letters, 2018. **229**: p. 48-52.

39. Han, M., Y. Mu, and J. Yu, *Nanoscopically and uniformly distributed SnO 2@ TiO 2/C composite with highly mesoporous structure and bichemical bonds for enhanced lithium ion storage performances.* Materials Advances, 2020. **1**(3): p. 421-429.

40. Tian, Q., et al., *Fabrication of novel hetero-nanostructure of SnO2@ TiO2@ C for improved lithium storage.* Materials Letters, 2017. **209**: p. 197-200.

41. Lu, Y., et al., *Centrifugally Spun SnO2 Microfibers Composed of Interconnected Nanoparticles as the Anode in Sodium-Ion Batteries.* ChemElectroChem, 2015. **2**(12): p. 1947-1956.

42. Liu, M., et al., *TiN surface modified SnO 2 as an efficient anode material for lithium ion batteries.* New Journal of Chemistry, 2013. **37**(7): p. 2096-2102.

43. Agubra, V.A., et al., *ForceSpinning of polyacrylonitrile for mass production of lithium-ion battery separators.* Journal of applied polymer science, 2016. **133**(1).

44. Zuniga, L., et al., *Multichannel hollow structure for improved electrochemical performance of TiO2/Carbon composite nanofibers as anodes for lithium ion batteries.* Journal of Alloys and Compounds, 2016. **686**: p. 733-743.

45. Mao, X., T.A. Hatton, and G.C. Rutledge, *A review of electrospun carbon fibers as electrode materials for energy storage.* Current Organic Chemistry, 2013. **17**(13): p. 1390-1401.

46. Cai, M., et al., *Lithium ion battery separator with improved performance via side-by-side bicomponent electrospinning of PVDF-HFP/PI followed by 3D thermal crosslinking.* Journal of Power Sources, 2020. **461**: p. 228123.

47. Li, X., et al., *Electrospinning-based strategies for battery materials.* Advanced Energy Materials, 2021. **11**(2): p. 2000845.

48. Zaarour, B., L. Zhu, and X. Jin, *A review on the secondary surface morphology of electrospun nanofibers: formation mechanisms, characterizations, and applications.* ChemistrySelect, 2020. **5**(4): p. 1335-1348.

49. Li, T., et al., *Performance enhancement of Sn-Ti-C nanofibers anode for lithium-ion batteries via deep cryogenic treatment.* Journal of Solid State Electrochemistry, 2020. **24**(3): p. 781-793.

50. Javed, K., et al., *A review on graphene-based electrospun conductive nanofibers, supercapacitors, anodes, and cathodes for lithium-ion batteries.* Critical Reviews in Solid State and Materials Sciences, 2019. **44**(5): p. 427-443.

51. Fang, D., et al., *Hollow SnO2-ZnO hybrid nanofibers as anode materials for lithium-ion battery.* Materials Research Express, 2014. **1**(2): p. 025012.

52. Ji, H., et al., *Complementary stabilization by core/sheath carbon nanofibers/spongy carbon on submicron tin oxide particles as anode for lithium-ion batteries.* Journal of Power Sources, 2019. **413**: p. 42-49.

53. Sarkar, K., et al., *Electrospinning to forcespinning™.* Materials today, 2010. **13**(11): p. 12-14.

54. Lv, R., et al., *Poly (vinylidene fluoride)/poly (acrylonitrile) blend fibrous membranes by centrifugal spinning for high-performance lithium ion battery separators.* Journal of Applied Polymer Science, 2017. **134**(8).

55. Padilla-Gainza, V., et al., *Forcespinning technique for the production of poly (d, l-lactic acid) submicrometer fibers: Process–morphology–properties relationship.* Journal of Applied Polymer Science, 2019. **136**(22): p. 47643.

56. Chavez, R.O., T.P. Lodge, and M. Alcoutlabi, *Recent developments in centrifugally spun composite fibers and their performance as anode materials for lithium-ion and sodium-ion batteries.* Materials Science and Engineering: B, 2021. **266**: p. 115024.

57. Chavez, R.O., et al., *Centrifugally spun carbon fibers prepared from aqueous poly (vinylpyrrolidone) solutions as binder-free anodes in lithium-ion batteries.* Journal of Applied Polymer Science: p. 50396.

58. Jia, H., et al., *High-performance SnSb@ rGO@ CMF composites as anode material for sodium-ion batteries through high-speed centrifugal spinning.* Journal of Alloys and Compounds, 2018. **752**: p. 296-302.

59. Agubra, V.A., et al., *Forcespinning: A new method for the mass production of Sn/C composite nanofiber anodes for lithium ion batteries.* Solid State Ionics, 2016. **286**: p. 72-82.

60. Valdez, A., *Forcespinning of Metal Oxides and Metal Sulfides and Their Applications as Alternative Anode Materials for Lithium-ion and Sodium-ion Batteries*. 2018: The University of Texas Rio Grande Valley.

61. Atıcı, B., C.H. Ünlü, and M. Yanilmaz, *A Review on Centrifugally Spun Fibers and Their Applications.* Polymer Reviews, 2021: p. 1-64.

62. Akia, M., et al., *In situ synthesis of Fe 3 O 4-reinforced carbon fiber composites as anodes in lithium-ion batteries.* Journal of Materials Science, 2019. **54**(21): p. 13479-13490.

63. Lu, Y., et al., *Comparing the structures and sodium storage properties of centrifugally spun SnO 2 microfiber anodes with/without chemical vapor deposition.* Journal of Materials Science, 2016. **51**(9): p. 4549-4558.

64. Theivaprakasam, S., et al., *Passivation behaviour of aluminium current collector in ionic liquid alkyl carbonate (hybrid) electrolytes.* NPJ Materials Degradation, 2018. **2**(1): p. 13.

65. Mauger, A., H. Xie, and C.M. Julien, *Composite anodes for lithium-ion batteries: status and trends.* 2016.

66. De las Casas, C. and W. Li, *A review of application of carbon nanotubes for lithium ion battery anode material.* Journal of Power Sources, 2012. **208**: p. 74-85.

67. Ji, L., et al., *α-Fe2O3 nanoparticle-loaded carbon nanofibers as stable and high-capacity anodes for rechargeable lithium-ion batteries.* ACS applied materials & interfaces, 2012. **4**(5): p. 2672-2679.

68. Wu, C., et al., *Fe2O3 nanorods/carbon nanofibers composite: Preparation and performance as anode of high rate lithium ion battery.* Journal of Power Sources, 2014. **251**: p. 85-91.

69. Luo, L., et al., *Electrospun ZnO–SnO2 composite nanofibers with enhanced electrochemical performance as lithium-ion anodes.* Ceramics International, 2016. **42**(9): p. 10826-10832.

70. Tran, T., et al., *Electrospun SnO2 and TiO2 composite nanofibers for lithium ion batteries.* Electrochimica Acta, 2014. **117**: p. 68-75.

71. Chen, K., et al., *SnO2 nanoparticles/TiO2 nanofibers heterostructures: In situ fabrication and enhanced gas sensing performance.* Solid-State Electronics, 2019. **157**: p. 42-47.

72. Kongsong, P., et al., *Photocatalytic antibacterial performance of glass fibers thin film coated with N-doped SnO2/TiO2.* The Scientific World Journal, 2014. **2014**.

73. Cheong, J.Y., et al., *Incorporation of amorphous TiO2 into one-dimensional SnO2 nanostructures as superior anodes for lithium-ion batteries.* Journal of Power Sources, 2018. **400**: p. 485-492.

74. Zuniga, L., et al., *Centrifugally spun α-Fe2O3/TiO2/carbon composite fibers as anode materials for lithium-ion batteries.* Applied Sciences, 2019. **9**(19): p. 4032.

75. Zhang, X. and Y. Lu, *Centrifugal spinning: an alternative approach to fabricate nanofibers at high speed and low cost.* Polymer Reviews, 2014. **54**(4): p. 677-701.

76. Weng, B., et al., *Fibrous cellulose membrane mass produced via forcespinning® for lithium-ion battery separators.* Cellulose, 2015. **22**(2): p. 1311-1320.

77. Kim, D., et al., *Electrospun Ni-added SnO2–carbon nanofiber composite anode for high-performance lithium-ion batteries.* ACS applied materials & interfaces, 2012. **4**(10): p. 5408-5415.

78. Tanguy, N.R., et al., *Facile one-pot synthesis of water-dispersible phosphate functionalized reduced graphene oxide toward high-performance energy storage devices.* Chemical Communications, 2020. **56**(9): p. 1373-1376.

79. Wan, N., et al., *Improved Li storage performance in SnO 2 nanocrystals by a synergetic doping.* Scientific reports, 2016. **6**(1): p. 1-11.

80. Subasri, R. and T. Shinohara, *Investigations on SnO2–TiO2 composite photoelectrodes for corrosion protection.* Electrochemistry Communications, 2003. **5**(10): p. 897-902.

81. Toloman, D., et al., *Photocatalytic activity of SnO2-TiO2 composite nanoparticles modified with PVP.* Journal of colloid and interface science, 2019. **542**: p. 296-307.

82. Wu, J.-M., H.C. Shih, and W.-T. Wu, *Formation and photoluminescence of single-crystalline rutile TiO2 nanowires synthesized by thermal evaporation.* Nanotechnology, 2005. **17**(1): p. 105.

83. Su, C., B.-Y. Hong, and C.-M. Tseng, *Sol–gel preparation and photocatalysis of titanium dioxide.* Catalysis Today, 2004. **96**(3): p. 119-126.

84. Kwoka, M. and M. Krzywiecki, *Impact of air exposure and annealing on the chemical and electronic properties of the surface of SnO2 nanolayers deposited by rheotaxial growth and vacuum oxidation.* Beilstein journal of nanotechnology, 2017. **8**(1): p. 514-521.

85. Babu, B., et al., *Bandgap tuning and XPS study of SnO2 quantum dots.* Materials Letters, 2018. **221**: p. 211-215.

86. Pal, B., et al., *Large scale synthesis of 3D nanoflowers of SnO2/TiO2 composite via electrospinning with synergistic properties.* Materials Letters, 2018. **225**: p. 117-121.

87. Erdem, B., et al., *XPS and FTIR surface characterization of TiO2 particles used in polymer encapsulation.* Langmuir, 2001. **17**(9): p. 2664-2669.

88. Södergren, S., et al., *Lithium intercalation in nanoporous anatase TiO2 studied with XPS.* The Journal of Physical Chemistry B, 1997. **101**(16): p. 3087-3090.

89. Kwan, Y.C.G., G.M. Ng, and C.H.A. Huan, *Identification of functional groups and determination of carboxyl formation temperature in graphene oxide using the XPS O 1s spectrum.* Thin Solid Films, 2015. **590**: p. 40-48.

90. Socratous, J., et al., *Electronic structure of low-temperature solution-processed amorphous metal oxide semiconductors for thin-film transistor applications.* Advanced functional materials, 2015. **25**(12): p. 1873-1885.

91. Wei, Z., et al., *Facile synthesis of Sn/TiO2 nanowire array composites as superior lithium-ion battery anodes.* Journal of power sources, 2013. **223**: p. 50-55.

92. Wang, D., et al., *Hierarchical nanostructured core–shell Sn@ C nanoparticles embedded in graphene nanosheets: spectroscopic view and their application in lithium ion batteries.* Physical Chemistry Chemical Physics, 2013. **15**(10): p. 3535-3542.

93. Kaplan, R., et al., *Simple synthesis of anatase/rutile/brookite TiO2 nanocomposite with superior mineralization potential for photocatalytic degradation of water pollutants.* Applied Catalysis B: Environmental, 2016. **181**: p. 465-474.

94. Liu, Q., et al., *3D branched rutile TiO2@ rutile SnO2 nanorods array heteroarchitectures/carbon cloth with an adjustable band gap to enhance lithium storage reaction kinetics for flexible lithium-ion batteries.* Electrochimica Acta, 2020. **354**: p. 136727.

95. Wang, W., et al., *SnO2/TiO2 nanocomposite prepared by pulsed laser deposition as anode material for flexible quasi-solid-state lithium-ion batteries.* International Journal of Electrochemical Science, 2020. **15**(12): p. 11709-11722.

96. Zou, L., et al., *A film of porous carbon nanofibers that contain Sn/SnOx nanoparticles in the pores and its electrochemical performance as an anode material for lithium ion batteries.* Carbon, 2011. **49**(1): p. 89-95.

97. Xu, Y., et al., *Uniform nano-Sn/C composite anodes for lithium ion batteries.* Nano letters, 2013. **13**(2): p. 470-474.

# BIOGRAPHICAL SKETCH

Gabriel Gonzalez was born in Mission, Texas in August 17, 1997 where he currently resides at 301 S Inspiration Rd, Mission, Texas, 78572. However, for the first 9 years of his life, Gabriel was raised in Reynosa and Rio Bravo, Tamaulipas, Mexico. At the age of 10, Gabriel's mother decided to move to the United States in the hopes of a better future. Gabriel's interest for math and science begun in the 5$^{th}$ grade when he was pronounced student of the year at his elementary. His science teacher at the time, Mr. Coronado, would always encourage him to believe in himself and aim for greatness. In 2012 Gabriel enrolled at Mission High School but due to personal issues transferred to Donna High School in 2014. It was there where his counselor and math teacher encouraged him to apply for a dual enrollment engineering academy (DEEA) with South Texas College (STC). In 2017 due to a tragic event, Gabriel transferred back to Mission High School where he graduated as the fifth ranking student of his class, an engineering associate's degree from STC, and a full ride to college. Gabriel completed his undergraduate studies in Mechanical Engineering at The University of Texas Rio Grande in December 2018 and his master's degree in Mechanical Engineering with specialization in Materials Science Engineering in May 2021. Gabriel can be contacted via e-mail at gabriel_gonzalez9094@outlook.com